The Journal of Undergraduate Research in Physics

CONTENTS

Volume 17, Number 1
Fall, 1998

Produced by the Physics Department of Guilford College
for
The American Institute of Physics and the Society of Physics Students

THE JOURNAL OF UNDERGRADUATE RESEARCH IN PHYSICS

This journal is devoted to research work done by undergraduate students in physics and its related fields. It is to be a vehicle for the exchange of ideas and information by undergraduate students. Information for students wishing to submit manuscripts for possible inclusion in the Journal follows.

ELIGIBILITY
The author(s) must have performed all work reported in the paper as an undergraduate student(s). The subject matter of the paper is open to any area of pure or applied physics or physics related field.

SPONSORSHIP
Each paper must be sponsored by a full-time faculty member of the department in which the research was done. A letter from the sponsor, certifying that the work was done by the author as an undergraduate and that the sponsor is willing to be acknowledged at the end of the paper, must accompany the manuscript if it is to be considered for publication.

SUBMISSION
Two copies of the manuscript, the letter from the sponsor and a telephone number or E-Mail address where the author can be reached should be sent to:
Dr. Rexford E. Adelberger, Editor
THE JOURNAL OF UNDERGRADUATE RESEARCH IN PHYSICS
Physics Department
Guilford College
Greensboro, NC 27410

FORM
The manuscript should be typed, double spaced, on 8 1/2 x 11 inch sheets. Margins of about 1.5 inches should be left on the top, sides, and bottom of each page. Papers should be limited to fifteen pages of text in addition to an abstract (not to exceed 250 words) and appropriate drawings, pictures, and tables. Manuscripts may be submitted on a disk that can be read by a MacIntosh™. The files must be compatible with MacWrite™, MicroSoft Word™ , PageMaker™ or WordPerfect™.

ILLUSTRATIONS
Line drawings should be made with black ink on plain white paper. The line thickness should be sufficient to be reduced to column format. Each figure or table must be on a separate sheet. Photographs must have a high gloss finish. If the submission is on a disk, the illustrations should be in PICT, TIFF or EPS format.

CAPTIONS
A descriptive caption should be provided for each illustration or table, but it should not be part of the figure. The captions should be listed together at the end of the manuscript

EQUATIONS
Equations should appear on separate lines, and may be written in black ink. All equations should be numbered. We use EXPRESSIONIST™ to format equations in the Journal.

FOOTNOTES
Footnotes should be typed, double spaced and grouped together in sequence at the end of the manuscript.

PREPARING A MANUSCRIPT
A more detailed set of instructions for authors wishing to prepare manuscripts for publication in the Journal of Undergraduate Research in Physics can be found in the back of each issue.

SUBSCRIPTION INFORMATION

The Journal is published twice each academic year, issue # 1 appearing in the fall and issue # 2 in the spring of the next calendar year. There are two issues per volume.

TYPE OF SUBSCRIBER	PRICE PER VOLUME
Individual	$US 5.00
Institution	$US 10.00

Foreign subscribers add $US 2.00 for surface postage, $US 10.00 for air freight.

Back issues may be purchased by sending $US 15.00 per volume to the editorial office.

To receive a subscription, send your name, address, and check made out to **The Journal of Undergraduate Research in Physics (JURP)** to the editorial office:

JURP
Physics Department
Guilford College
Greensboro, NC 27410

The Journal of Undergraduate Research in Physics is sent to each member of the Society of Physics Students as part of their annual dues.

VOLUME 17

ACADEMIC YEAR 1998-1999

The Journal of Undergraduate Research in Physics

Produced by the Physics Department
of Guilford College
for
The American Institute of Physics
and
The Society of Physics Students

ISSN 0731 - 3764

TWO LASER EXCITATION OF A THREE STATE ATOM

Emek Yesilada *
Department of Physics and Astronomy
University of Rochester
Rochester, NY 14627

ABSTRACT

We determine the complex eigenvalues of a laser-driven three state quantum system. These eigenvalues are used to determine the photon absorption rate.

INTRODUCTION

In our model, we consider two different types of three-level atoms that interact with photons. A 'cascade' atom is one where an atom is excited to a second higher energy level by absorption of a photon and then is excited to a third even higher energy level by absorption of a second photon (see Figure 1a). In contrast, a 'lambda' atom absorbs a photon, exciting it to the highest energy level and then the atom reaches a third level, that has less energy, by stimulated emission caused by a second photon. (see Figure 1b). In both cases, the two transition energies in each of the atoms are assumed to be quite different, so two different energy lasers are needed to supply the required pairs of photons to interact with the three level atoms. The energies of the photons produced by the two lasers are labeled $\hbar\omega_a$ and $\hbar\omega_b$ as shown in Figure 1.

For the interactions between the photons and the atom to occur, the photon energies do not have to exactly match the energy difference between the states of the atom. The difference between the photon energy and the energy between energy states of the atom is characterized by a 'detuning' shown as $\hbar\Delta_2$ and $\hbar\Delta_3$ as shown in Figure 2. The success of the transitions, whether the photons actually can excite the atoms, depends on the detunings. The larger the detunings become, the more difficult it gets for the atoms to make the transitions.

The second energy level, because of collisions with other atoms, can undergo a non-radiative transition to a lower energy state. This sort of process can be handled by making Δ_2 have an imaginary part. There is an indirect loss process for all other levels as well. We will examine this loss process in detail when we find the eigenvalues for the various states.

Emek is a first year graduate student working with an experimental atomic and molecular phhysics group at the University of Texas at Austin. This research was begun in the spring of 1997 at the University of Rochester. He loves playing soccer and is enjoying the sunny days of Texas.

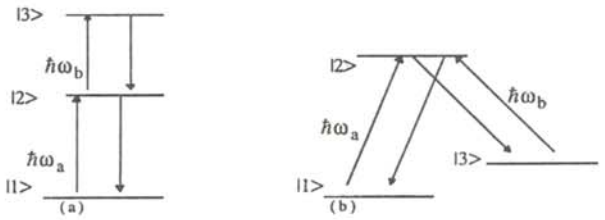

Figure 1

Sketches of two types of 3 level atoms, where ω_a and ω_b are the frequencies of the lasers a and b respectively. a) shows a cascade atom; b) shows a lambda atom.

Solving Schrödinger's Equation

We must solve the time dependent Schrödinger equation to determine the transition rates. The transition rates depend on the size of the detunings, the strength of the laser fields and the dipole moments of the atoms. The Hamiltonian is a sum of two terms: $H = H_A + H_{Int}$ representing the bare atom and the atom's interaction with the laser field.

Because the atom being considered has just three states,

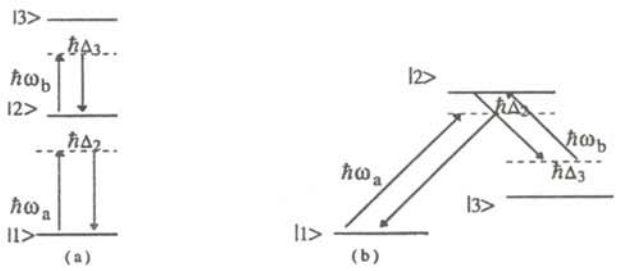

Figure 2

Sketches of the two types of 3 level atoms showing the energy gaps Δ_2 and Δ_3.

the Hamiltonian will be a 3x3 matrix. The ij^{th} element of the Hamiltonian is:

$$< i|H|j > = < i|H_A + H_{Int}|j > = < i|W_j|j > + < i|H_{Int}|j >$$
$$= W_j \delta_{ij} + < i|H_{Int}|j > , \quad (1)$$

where W_j is the energy of the j^{th} state of the atom and δ_{ij} is the Kroeneker delta.

The wavefunction, $\Psi(t)$ for the three state system is a linear combination of the three states: [1]

$$\Psi(t) = c_1(t)\,|1> + c_2(t)\,|2> + c_2(t)\,|2> , \quad (2)$$

where |1>, |2> and |3> are the eigenfunctions for the three states of the atom.

The Schrödinger equation, in matrix form, for this system is: [2]

$$i\hbar\frac{\partial\Psi}{\partial t} = H\Psi$$

$$i\hbar\frac{d}{dt}\begin{bmatrix} c_1 \\ c_2 \\ c_3 \end{bmatrix} = \begin{bmatrix} <1|H|1> & <1|H|2> & <1|H|3> \\ <2|H|1> & <2|H|2> & <2|H|3> \\ <3|H|1> & <3|H|2> & <3|H|3> \end{bmatrix}\begin{bmatrix} c_1 \\ c_2 \\ c_3 \end{bmatrix} \quad (3)$$

To evaluate the term $<1|H|2>$ note that from Equation 1, $<1|H_A|2> = W_1$. The term that describes the interaction with the laser photon is a bit more complicated:

$$<1|H_{Int}|2> = -d_{12}\,[E_a(t) + E_b(t)] , \quad (4)$$

where $d_{12} = \int \phi_1(r)\,[er]\,\phi_2(r)\,d^3r$, e is the electron charge, ϕ_1 and ϕ_2 are the eigenstates if there were no laser interaction and E_a and E_b are the electric fields of the two lasers. The electric field due to the two lasers is given by:

$$E_a(t) = E_a \exp[-i\omega_a t] + E_a^* \exp[i\omega_a t]$$
$$E_b(t) = E_b \exp[-i\omega_b t] + E_b^* \exp[i\omega_b t] , \quad (5)$$

where E_a and E_b are the complex peak laser field strengths. We will assume that the fields are monochromatic, so E_a and E_b are real and independent of time.

To eliminate the main time dependence of the Hamiltonian, we define:

$$c_1 = a_1 \exp\left[-i\frac{W_1}{\hbar}t\right]$$
$$c_2 = a_2 \exp\left[-i\left(\omega_a + \frac{W_1}{\hbar}\right)t\right] \quad (6)$$
$$c_3 = a_3 \exp\left[-i\left(\omega_a \pm \omega_b + \frac{W_1}{\hbar}\right)t\right] .$$

If the frequency term in c_3 is $(\omega_a + \omega_b)$, we have a 'cascade' atom; if the frequency term in c_3 is $(\omega_a - \omega_b)$, we have a 'lambda' atom.

To show that the Hamiltonian becomes mainly independent of time and the energy W_i of the three levels , we work out an example for both c and a. Consider the equation of c_2 (from Equation 3):

$$i\hbar\frac{\partial}{\partial t}c_2 = <2|H|1>c_1 + <2|H|2>c_2 + <2|H|3>c_3 \quad (7)$$

Using Equation 4:

$$i\hbar\frac{\partial}{\partial t}c_2 =$$
$$-(d_{12})^*\left\{E_a e^{[-i\omega_a t]} + E_a e^{[i\omega_a t]} + E_b e^{[-i\omega_b t]} + E_b e^{[i\omega_b t]}\right\}c_1 + W_2 c_2$$
$$-(d_{23})\left\{E_a e^{[-i\omega_a t]} + E_a e^{[i\omega_a t]} + E_b e^{[-i\omega_b t]} + E_b e^{[i\omega_b t]}\right\}c_3 . \quad (8)$$

Now, if we substitute in the expressions for the c's from Equation 6, Equation 8 becomes:

$$i\hbar\frac{\partial a_2}{\partial t}e^{-i\left(\omega_a + \frac{W_1}{\hbar}\right)t} =$$
$$-(d_{12}) * \{E_a e^{[-i\omega_a t]} + E_a e^{[i\omega_a t]} + E_b e^{[-i\omega_b t]} + E_b e^{[i\omega_b t]}\}\,a_1 e^{-i\frac{W_1}{\hbar}t}$$
$$+\left\{W_2 - \hbar\omega_a - W_1\right\}a_2 e^{-i\left(\omega_a + \frac{W_1}{\hbar}\right)t} - \quad (9)$$
$$(d_{12})\{E_a e^{[-i\omega_a t]} + E_a e^{[i\omega_a t]} + E_b e^{[-i\omega_b t]} + E_b e^{[i\omega_b t]}\}a_1 e^{-i\left(\omega_a \pm \omega_b + \frac{W_1}{\hbar}\right)t}$$

Recalling the definition of the detuning parameters Δ_2 and Δ_3, and doing some further simplification, such as ignoring terms involving $\exp[2i\omega_a t]$, $\exp[i(\omega_a + \omega_b)t]$ and even $\exp[i(\omega_a - \omega_b)t]$ as they oscillate very rapidly and will have no long term effect on the system, Equation 9 can be written as:

$$i\hbar\frac{\partial a_2}{\partial t} = -(d_{12}) * E_a a_1 + \hbar\Delta_2 a_2 - d_{23}E_b . \quad (10)$$

The reader should also note that $W_2 = W_1 + \hbar\omega_a + h\Delta_2$.

In a similar fashion we can obtain two equations for $\frac{\partial a_1}{\partial t}$ and $\frac{\partial a_3}{\partial t}$ which are a bit simpler as $<1|H|3>$ and $<3|H|1>$ are both zero by the selection rule. We do not allow any transitions from the first to the third state and vice versa.

If we let:

$$a = \frac{d_{12}E_a}{\hbar} = \frac{\left(d_{12}E_a\right)^*}{\hbar} \quad \text{and} \quad b = \frac{d_{23}E_b}{\hbar} = \frac{\left(d_{23}E_b\right)^*}{\hbar} \quad (11)$$

the Schrödinger equation takes on the form:

$$i\frac{\partial}{\partial t}\begin{bmatrix} a_1 \\ a_2 \\ a_3 \end{bmatrix} = \begin{bmatrix} 0 & -a & 0 \\ -a & \Delta_2 & -b \\ 0 & -b & \Delta_2 \pm \Delta_3 \end{bmatrix}\begin{bmatrix} a_1 \\ a_2 \\ a_3 \end{bmatrix} . \quad (12)$$

If the last element of the Hamiltonian is $\Delta_2 + \Delta_3$, we have a cascade atom, if the last element is $\Delta_2 - \Delta_3$, we have a lambda atom.

In the special case where $a = b$, we can factor out a in Equation 12 to make the matrix dimensionless. If we define $d_2 = \Delta_2/a$ and $d_3 = \Delta_3/a$, Equation 12 now takes on the form:

$$i\frac{\partial}{\partial t}\begin{bmatrix} a_1 \\ a_2 \\ a_3 \end{bmatrix} = a\begin{bmatrix} 0 & -1 & 0 \\ -1 & d_2 & -1 \\ 0 & -1 & d_2 \pm d_3 \end{bmatrix}\begin{bmatrix} a_1 \\ a_2 \\ a_3 \end{bmatrix}. \qquad (13)$$

The most important feature of this result is that in contrast to Equation 3, the Hamiltonian matrix is now independent of time.

Eigenvalues, Analytic Approximations

If we denote the Hamiltonian matrix in Equation 13 by M and the eigenvector by Φ, we have:

$$M\,\Phi = \lambda\, I\,\Phi\,, \qquad (14)$$

where λ is the eigenvalue of M and I is the identity matrix. The eigenvalue in Equation 14 will be different from the bare atomic energies W_1, W_2 and W_3 due to the interactions of the laser. Equation 14 has nontrivial solutions when:

$$\det(M-\lambda I) = \begin{vmatrix} \lambda & 1 & 0 \\ 1 & \lambda - d_2 & 1 \\ 0 & 1 & \lambda-(d_2 \pm d_3) \end{vmatrix} = 0\,. \qquad (15)$$

If we denote the last element as $\delta = d_2 \pm d_3$, solving Equation 15 gives the cubic equation:

$$\lambda^3 - \lambda^2(\delta + d_2) + \lambda(d_2\,\delta - 2) + \delta = 0\,. \qquad (16)$$

We first obtain the eigenvalues for particular values of d_2 and d_3. When $\delta = 0$, one of the eigenvalues will be zero. When δ and d_2 are very large, we can simply ignore the subscripts representing the laser field strengths a and b. In this case, Equation 15 is already diagonal, giving the eigenvalues 0, d_2 and δ.

The laser frequencies, ω_a and ω_b, and the detunings are assumed to be under the control of the experimenter. To show what happens for different choices of the dimensionless detunings d_2 and d_3, we introduce a control parameter z, such that:

$$d_2 = -1 + z \quad \text{and} \quad d_3 = -5 + z\,. \qquad (17)$$

When $z = 0$, $d_2 = -1$ and $d_3 = -5$, meaning that the laser field strength is greater than the energy needed for the transition. As z increases, the detunings become less negative and eventually positive, meaning that the laser has less than the energy required for the transitions. One photon exact resonances occur when $z = 1$ ($d_2 = 0$) and when $z = 5$ (d_3=0). If we are considering a lambda atom, we set $d_3 = 5 - z$ because in this case, the third level is reached by stimulated emission rather than by an absorption.

If the detuning parameters can have a real and imaginary part, we define the complex parameter as $\bar{d}_2 = d_2 - i\gamma$. The characteristic equation (Equation 16):

$$\lambda^3 - \lambda^2(\delta + \bar{d}_2) + \lambda(\bar{d}_2\,\delta - 2) + \delta = 0\,. \qquad (18)$$

has complex eigenvalues as solutions.

There are several interesting regions depending on which parameter is taken as small. When $\bar{d}_2 >> \delta$ and δ is very small, we can scale Equation 18 by dividing by $(\bar{d}_2)^3$. Making the substitution:

$$x = \frac{\lambda}{\bar{d}_2},\; y = \frac{\delta}{\bar{d}_2},\; A = \frac{1}{\bar{d}_2}\,. \qquad (19)$$

Equation 18 becomes.

$$x^3 - x^2(y+1) + x(y - 2A^2) + A^2 y = 0 \qquad (20)$$

To examine the behavior of x and λ near zero, we set:

$$x = \alpha y + \beta y^2 + \theta y^3, \qquad (21)$$

and insert Equation 21 into Equation 20. The coefficients of y, y^2 and y^3 are set to zero to determine α, β and θ. When we substitute the calculated values of α, β and θ into Equation 21, we get:

$$x = \frac{1}{2}y + \frac{1}{8A^2}y^2 - \frac{1}{16A^2}y^3\,. \qquad (22)$$

Putting Equation 22 back into Equation 19, λ becomes:

$$\lambda = \frac{1}{2}\delta + \frac{1}{8}\bar{d}_2\,\delta^2 - \frac{1}{16}\delta^3 \qquad (23)$$

Equation 23 shows that when the eigenvalue λ is small, its imaginary part has only even powers of δ. When we use Equation 18 to plot the imaginary part of λ for small λ and δ, a parabolic behavior results as shown in Figure 4.

Another interesting case is that when δ is large. Then we can introduce a dimensionless scaling by dividing Equation 18 by δ^3. For the eigenvalue near zero, we do a similar analysis as with the case for small δ:

$$\lambda = -\frac{1}{\bar{d}_2} = -\frac{d_2}{d_2^2 + \gamma^2} - i\frac{\gamma}{d_2^2 + \gamma^2}\,. \qquad (24)$$

To analyze the eigenvalue close to δ, we set

$$\lambda = \delta + \varepsilon\,, \qquad (25)$$

where ε is the small parameter. Inserting Equation 25 into Equation 18 and keeping only terms linear in ε and going through an analysis similar to the one done to get Equation

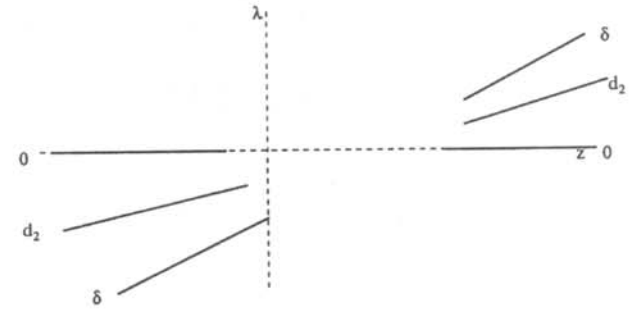

Figure 3
Sketch of the eigenvalues for large δ and d_2. The control parameter z is given in Equation 17. The blank central region is shown in Figure 5.

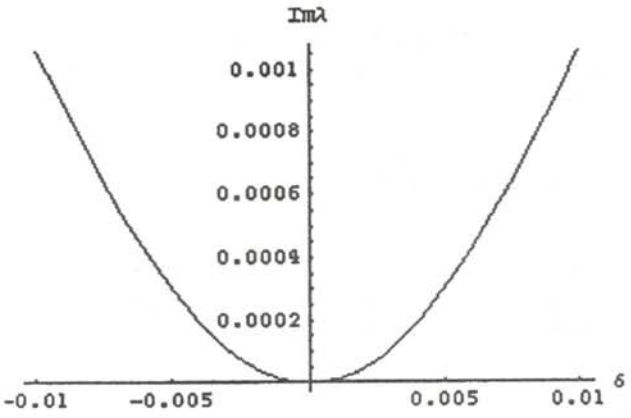

Figure 4
Plot of the negative of the Imaginary part of the eigenvalue for d_2 = 10 and γ = 1 as a function of δ.

24:

$$\varepsilon = \frac{1}{\delta - \tilde{d}_2} = \frac{\delta - d_2}{d_3^2 + \gamma^2} - i\frac{\gamma}{d_3^2 + \gamma^2}. \qquad (26)$$

Substituting Equation 26 into Equation 25, we find that the imaginary part of the eigenvalue λ is:

$$\mathrm{Im}\,\lambda = -\frac{\gamma}{d_3^2 + \gamma^2}. \qquad (27)$$

To find the behavior of the eigenvalue close to $\tilde{d}_2$, we write:

$$\lambda = \tilde{d}_2 + \varepsilon. \qquad (28)$$

Again performing a similar analysis, the imaginary part of the eigenvalue λ is:

$$\mathrm{Im}\,\lambda = -\gamma + \frac{2\gamma}{d_3^2 + \gamma^2}. \qquad (29)$$

Two (for near δ and for large δ) of the imaginary parts of the eigenvalue decrease and approach zero with increasing d, and one (near $\tilde{d}_2$) approaches the steady value of $-\gamma$ in its asymptotic limit (see Equation 29).

NUMERICAL RESULTS

We used MATHEMATICA™ to obtain numerical values for the eigenvalues in the region where δ is small (the region that was left blank in Figure 3. Graphs of the value of the eigenvalue as a function of z (see Equation 17) with γ = 1 are shown in Figure 5. Note that the numerical values of the eigenvalues come very close to each other at three points called 'avoided crossings'. We had to tell MATHEMATICA™ to order the eigenvalues by size to avoid any jumping from one eigenvalue to the other at these 'avoided crossings'. Figure 6 shows the results for the imaginary values of the eigenvalues.

ABSORPTION RATE

The ground state probability amplitude is of the form:

$$a_1(t) = A_1 e^{-i\lambda_1 t} + A_2 e^{-i\lambda_2 t} + A_3 e^{-i\lambda_3 t}, \qquad (30)$$

where λ_1, λ_2 and λ_3 are the three eigenvalues. The three terms in Equation 30 will be decaying at different rates as the λ's have different imaginary parts. The term with the smallest imaginary part of the eigenvalue decays the slowest. Thus, the ground state probability can be written as:

$$|a_1(t)|^2 = |A|^2 e^{-2\lambda_{SI} t}, \qquad (31)$$

where λ_{SI} is the smallest imaginary part of the three eigenvalues. Taking the derivative of Equation 31 shows that the speed of the decay is determined by λ_{SI}, which is called the 'absorption rate'. Note that the absorption rate is just the negative of the decay rate or $-\lambda_{SI}$.

The imaginary parts of the eigenvalues represent the speed at which the population decays. We are interested only in the smallest imaginary part as the others will already have decayed. Figure 6 shows that the imaginary parts cross each other at certain points. At these points, the absorption rate is not represented by the imaginary part of a single eigenvalue throughout the whole range. So, we tell MATHEMATICA™ to take the smallest imaginary part throughout the entire range to give us the absorption rate, shown in Figure 7.

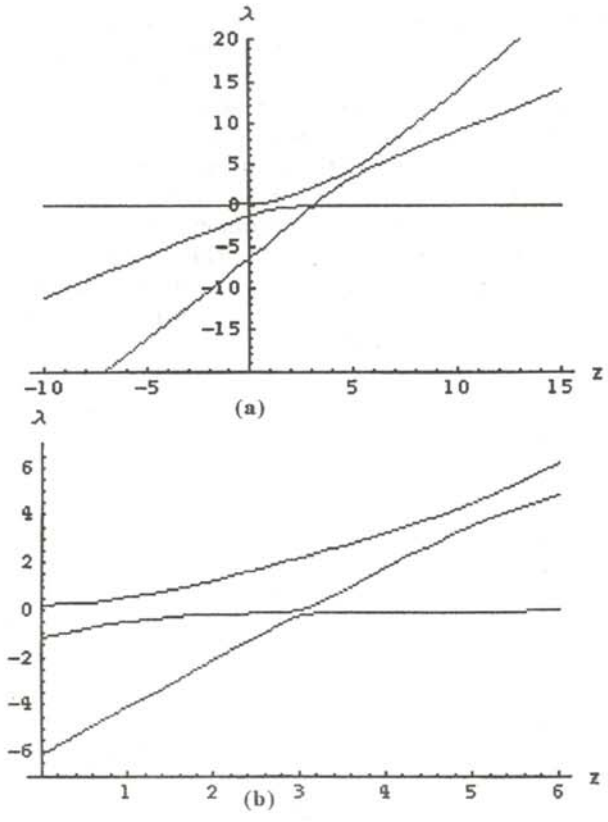

Figure 5
a) MATHEMATICA™ output to show the values of the eigenvalues in the region where d is small as a function of z (d_2 = -1+z, d_3 = -5 + z, γ = 1). b) A closer look to see the avoided crossings of the eigenvalues.

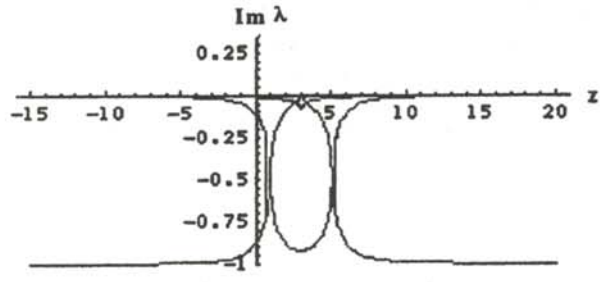

Figure 6
MATHEMATICA™ generated plot of the imaginary part of the eigenvalues as a function of z. Notice that the values cross at certain points.

'MAGIC' DOUBLE RESONANCE

The case where $\delta = d_2 + d_3 = 0$ is called double-photon resonance. From Figure 7 we see that when we have double-photon resonance, the absorption rate is zero. This was not expected because the higher the number of transitions, the higher the number of electrons lost. Here the detunings add up to zero. When the detunings are small, the transitions are more likely to happen.

At the double-photon resonance there is no loss of electrons even though the photon energies match with the transition energies. This means that when the atom is excited with two lasers that exactly match the atomic transitions, the second level (where the loss takes place) is skipped. As we move away from the resonance, there is a sudden increase in the absorption rate. If we go too far away from the resonance, the absorption rate starts decreasing and becomes very small. This can be seen from the asymptotic approximations of Equations 24 and 27. This is because when the detuning become very large, the transitions are not likely to occur.

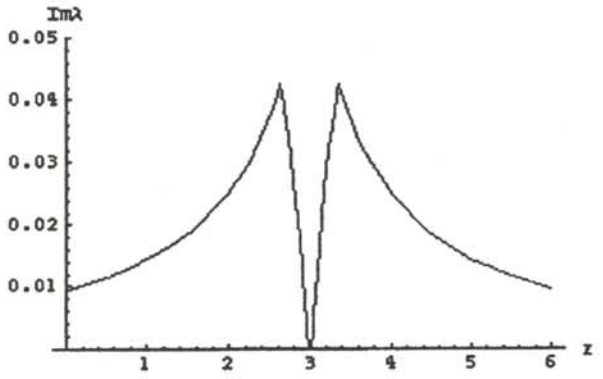

Figure 7
Absorption rate of photons as a function of the parameter z. ($\delta = d_2 + d_3 = 0$ at $z = 3$)

ACKNOWLEDGMENTS

This research was partially supported by NSF Grant PHY 97-22024.

REFERENCES

* Current address of author: Physics Deparatment, C1600, University of Texas, Austin, TX 78712

1. J.V. Ruffo., "Adiabatic Population Transfer in a Three-Level Atom", J. Undergrad. Res. Phys., 15, p. 26.
2. J.H. Eberly and P.W. Milonni, Encyclopedia of Physical Science and Technology, 11, pp. 474-477.

FACULTY SPONSOR

Dr. J.H. Eberly
Department of Physics and Astronomy
University of Rochester
Rochester, NY 14627

DESIGN OF A LOW COST GAMMA RAY SPECTROMETER TO INVESTIGATE SPECIAL RELATIVITY

James Bopp *
Division of Science (Physics)
Truman State University
Kirskville, MO 63501
received Sept 15, 1997

ABSTRACT

We designed a low cost NaI(Tl) scintillation detector and single channel analyzer to be used to measure the rest energy of the electron. We used the instrument to deduce the behavior of electrons following Compton scattering collisions in the crystal. We found a value of the rest energy of the electron to be (0.51±0.02) MeV and experimentally verified Einstein's energy-momentum relationship.

INTRODUCTION

The experimental investigation of special relativity in the undergraduate laboratory is often neglected due to the high cost and sophistication of instrumentation capable of measuring relativistic behavior. This means that many students feel that relativistic theory only applies to imaginary rockets traveling close to the speed of light and not to the real world. However, when studying the interaction between matter and gamma rays during events such as Compton scattering, one finds that relativistic behavior is the norm.

Gamma rays primarily interact with matter in three ways: a) via the photoelectric effect; b) via Compton scattering; and c) via pair production. The material we will be using in this experiment is a NaI(Tl) scintillation crystal, a material that converts the energy of an icident gamma ray into photons of visible light. In this paper, we will be concerned with the first two mechanisms.

Photoelectric Effect

The photoelectric effect is a phenomenon in which a photon (a gamma ray in this experiment) is absorbed by a tightly bound electron in the material. This electron is then ejected from the atom with an energy, E_e, equal to the difference between the photon energy, $E\gamma$, and the binding energy, E_B, of the electron to the atom.

$$E_e = E_\gamma - E_B \ . \qquad (1)$$

In a NaI(Tl) scintillation crystal, all of E_e is deposited in the crystal's lattice. E_B shows up as a X-ray from the filing of the vacancy in the atom created by the ejection of the electron. This X-ray is also absorbed by the crystal. Therefore, nearly all of the energy of the gamma ray interacting with the crystal through the photoelectric effect is deposited in the detector.

Figure 1 shows an idealized output from a scintillation crystal that is being bombarded by single energy gamma rays. The photopeak shown is caused by the photoelectric absorption in the crystal. This peak corresponds directly to the energy of the incident photon. [1]

Compton Scattering

Compton scattering is essentially a sub atomic game of billiards. An incident gamma ray interacts with a free electron and the two scatter as depicted in Figure 2. The energy of the original gamma ray is divided between the energy of the scattered gamma ray and the recoil electron in a way that conserves energy and momentum. The energy of the scattered gamma ray is dependent on the scattering angle. The scattered photon frequently escapes from the scintillation crystal and only the energy of the recoil electron is absorbed by the crystal and reemitted as visible light.

Compton scattering in the crystal produces a continuous spectrum in the output as shown in Figure 1. The Compton Continuum shows electrons with kinetic energy beginning at almost zero, the photon just grazing the electron and scattering at a small angle, to some maxi-

James earned a B.Sc. in physics from Truman State University in May of 1998 with minors in mathematics, philosophy and religion. The research discussed here was conducted during his last two years at Truman. It was sponsored by grants from the Univerisity. He is currently a Jesuit novice at St. Paul, MN. He hopes to study physics at the graduate level while he engages in the philosophical and theological studies necessary to become a Catholic priest.

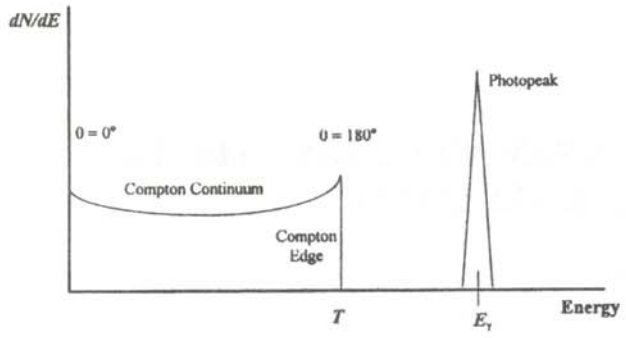

Figure 1
Idealized spectrum produced by a gamma ray stopping in a scintillating crystal. The photopeak corresponds to the energy of the incident gamma ray. The Compton edge corresponds to the maximum kinetic energy an electron can obtain through Compton scattering.

mum kinetic energy, T_{max}, known as the Compton Edge, where the photon back scatters at 180 degrees. [2] The energy corresponding to the Compton Edge can never equal the original energy of the photon because both energy and momentum are conserved in the interaction.

Relativistic Kinematics

Discussions on relativistic kinematics can be found in many textbooks. [3] Using the conservation of total energy and relativistic momentum, where:

$$E_e^{\,2} = (cp)^2 + (m_o c^2)^2 = (T + m_o c^2)^2 , \qquad (2)$$

where T is kinetic energy, the Compton edge energy, T_{max}, due to the scattering of a photon of energy $E\gamma$, is given by[4]:

$$T_{\max} = \frac{E_\gamma}{1 + 2\frac{E_\gamma}{m_o c^2}} . \qquad (3)$$

where m_oc^2 is the rest energy of the electron. Solving Equation 3 for the rest energy gives:

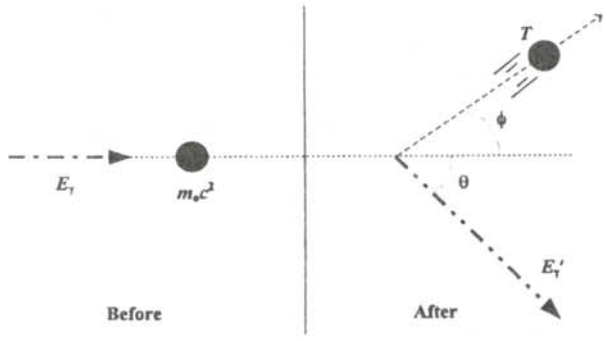

Figure 2
Schematic diagram of a Compton scattering event.

$$m_o c^2 = \frac{(cp)^2 - (T_{\max})^2}{2\,T_{\max}} = \frac{2\,E_\gamma\,(E_\gamma - T_{\max})}{T_{\max}} . \qquad (4)$$

When one analyzes the scattering from a classical nonrelativistic standpoint, Equation 4 would take the form:

$$\left(m_o c^2\right)_{classical} = \frac{(cp)^2}{2\,T_{\max}} = \frac{\left(2\,E_\gamma - T_{\max}\right)^2}{2\,T_{\max}} . \qquad (5)$$

Equations 4 and 5 only differ significantly when T_{max} becomes a significant fraction of the rest energy of the electron. Thus if one experimentally measures T_{max} and E_γ for gamma ray energies in the MeV region, one can experimentally verify the relativistic kinematics formulae.

THE APPARATUS

There is much information on how to apply gamma ray spectrometry to the study of special relativity. [5] The typical gamma ray spectrometer functions in the following way. A gamma ray enters the scintillating crystal where it interacts with the atoms in the crystal through the photoelectric effect or Compton scattering. In either case, the disturbance of the electrons in the crystal results in a flash of light whose intensity is directly proportional to the kinetic energy of the agitated electron. This flash of light is reflected into a photomultiplier tube (PMT) which uses photoelectric absorption and secondary emission to transform the light into an electrical pulse whose voltage magnitude is directly proportional to the intensity of the light, and therefore, proportional to the energy deposited by the gamma ray in the crystal.

What is unique about what we have done is the cost and simplicity of the apparatus. Traditional apparatus for gamma ray spectroscopy in the undergraduate laboratory consists of a scintillation detector (a scintillating crystal attached to a photomultiplier tube) which sends signals to a computer based multichannel analyzer. Others use high purity germanium detectors that must be stored and operated at cryogenic temperatures. In general, these systems cost thousands of dollars.

Our spectrometer is certainly more primitive than the commercially available models, but it is capable of obtaining comparable results for less than a thousand

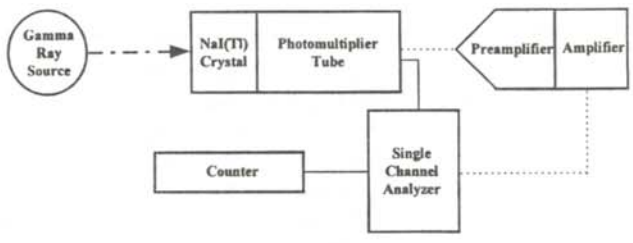

Figure 3
Schematic diagram of the electronics used to construct the Gamma Ray Spectrometer used in this experiment.

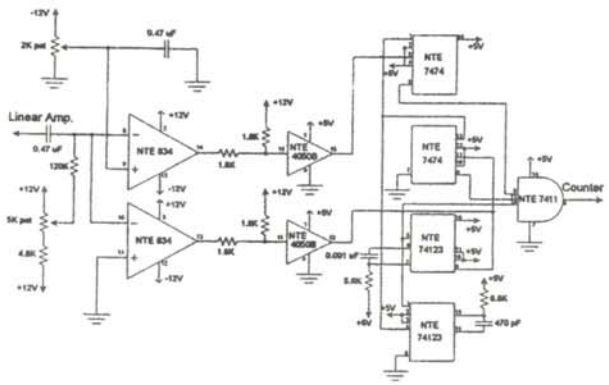

Figure 4
Schematic diagram of the Single Channel Analyzer

dollar investment. We purchased a 2" x 2" NaI(Tl) crystal and a 10 stage box and grid PMT [6] and a high voltage power supply to operate the PMT [7]. We built our own voltage divider for the PMT. The detector we constructed produced large signals (around 5 V for a 0.662 MeV gamma ray), so no preamplifier was necessary to analyze the signal. To analyze the various voltage pulses produced by the PMT, we built a single channel analyzer (SCA) out of five common integrated circuits and a few peripheral components. [8] Figure 4 is a schematic diagram of the SCA.

The SCA consists of a small fixed voltage window which is systematically swept through the full range of the possible voltages input to the device. Any pulse which falls above or below the window is blocked, while pulses whose peaks fall within the window produce a logic pulse which is sent to a counter. (see Figure 5).

The relative number of counts per time are plotted as a function of the voltage value of the center of the window. This histogram is called the gamma ray spectrum. Figure

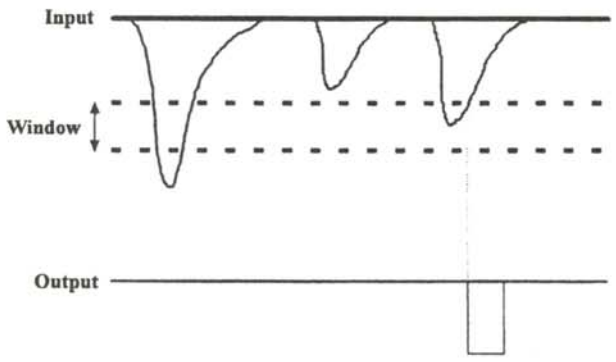

Figure 5
Basic operation of a single channel analyzer. Only those pulses whose peak value falls inside the window register cause a logic pulse to be sent to the counter.

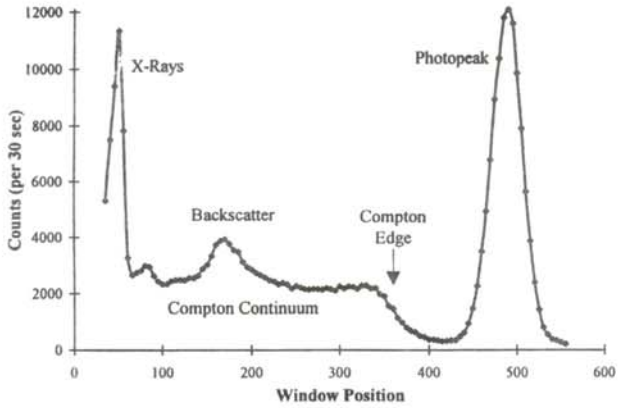

Figure 6
Experimental gamma ray spectrum for a 137Cs source. Compare this to Figure 1.

5 shows a spectrum we obtained from a ^{137}Cs source. It should be compared to the 'ideal' spectrum shown in Figure 1. The SCA is calibrated by producing gamma ray spectra for several sources that have known energy photopeaks and determining the energy value corresponding to any given window value (see Figure 6).

The total cost of our spectrometer was less than one thousand dollars. Our spectrometer has a resolution (FWHM, ^{137}Cs) of 7.7%, which is typical of commercial NaI(Tl) gamma ray spectrometers. The disadvantage of using an SCA is that it takes over an hour to collect the spectrum data using it.

RESULTS USING OUR SPECTROMETER

We carefully measured the gamma ray spectrum for 8 different sources. From these data, we determined values of the Compton edge (T_{max}) and the energy of the gamma ray ($E\gamma$). Table 1 shows these results.

Figure 7 is a plot of the rest energy vs T_{max} using Equation 5, the relativistically correct analysis of Compton Scattering. The zero slope fit to the data in Figure 8 shows an invariant rest mass with a value (0.51±0.02) MeV. This value overlaps the currently accepted value of the rest energy of the electron.

Figure 8 shows a plot of the momentum of the electron that is back scattered as a function of the measured kinetic energy (T_{max}). The solid line is what one would expect using the classical approximation. The dashed line in Figure 8 is the relativistically correct theoretical relationship between momentum and kinetic energy.

ACKNOWLEDGMENTS

The author would like to extend his special thanks to Dr. Kenneth Hahn for his guidance and advice. Thanks also go to Dr. Maria de Stefano for arranging the financial resources to build the spectrometer and to T.W. Sorrel for his work in the machine shop and Dr. Peter Jolivette for

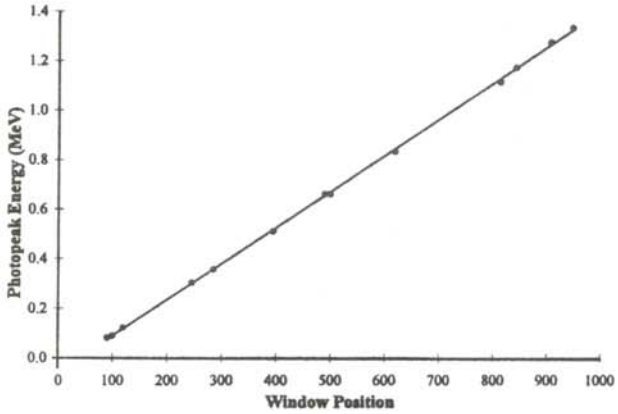

Figure 6
Calibration graph created by plotting known photopeak energies against measured photopeak positions. The line is a best fit using linear regression. The error bars are smaller than the data points.

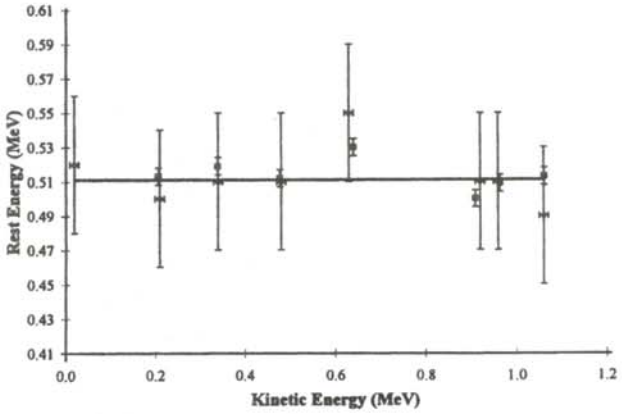

Figure 7
Relativistic calculations for the electron's rest energy plotted against its kinetic energy. The solid line is at 0.511 MeV. The square data points are from measurement taken with an HPGe detector and are shown for the sake of comparison.

allowing the use of his HPGe detector data.

REFERENCES

* Current address of the author: James L. Bopp, 19475 Countryside Circle, Weston MO, 64098,

1. W. R. Leo, Techniques for Nuclear and Particle Physics Experiment, Springer Verlag, New York, (1994), p. 54.
2. G.F. Knoll, Radiation Detection and Measurements, John Wiley & Sons, New York, (1989), p. 290-291.
3. J. Brehm and W. Mullin, Introduction to the Structure of Matter, John Wiley & Sons, new York, (1989), p. 107-110.
4. G. F. Knoll, Radiation Detection and Measurement, John Wiley & Sons, New York, (1989), p. 290.
5. The following articles all deal with Compton scattering as an approach to the study of special relativity: P.L. Jolivette and N. Rouze, Am. J. Phys., 57, (1989), pp. 822-825 (This is a very well done article which serves as the inspiration for this paper); M.J.U.H. Hoffman, Am. J. Phys., 57, (1989), pp. 822-825; T.S. Mudhole and N. Umakantha, Am. J. Phys., 45, (1970), pp. 1119 - 1120; J. Higbie, Am. J. Phys., 41, (1974), pp. 641-644.
6. Rexon Components, Inc., 24500 Highpoint Road, Beachwood, OH 44122. This cost is $600.
7. Bertan, 121 New South Road, Hicksville, NY 11801. The cost is $260.
8. The design of the SCA is a slight modification of that proposed by D. Parker and JU. French, Am. J. Phys., 53, (1985), pp. 793-794.
9. This data was obtained through correspondence with Dr. Jolivette, Hope College, Holland MI 49423.

Source	Experimental Photopeak Energy (MeV)	Accepted Photopeak Energy (MeV)	Experimental Compton Energy (MeV)
^{22}Na	1.265±.007	1.2745	1.06±.01
^{22}Na	0.511±.007	0.5110	0.34±.01
^{60}Co	1.171±.007	1.1732	0.96±.01
^{65}Zn	1.127±.007	1.1155	0.92±.01
^{54}Mn	0.838±.007	0.8340	0.63±.01
^{137}Cs	0.664±.007	0.6616	0.48±.01
^{133}Ba	0.358±.007	0.3560	0.21±.01
^{109}Cd	*0.083±007*	*0.0880*	*0.02±01*

Table 1
Measured and accepted values of the photopeak and our measured values for the Compton edge energies.

FACULTY SPONSOR

Professor Kenneth Hahn
Division of Science
Truman State University
Kirksville, MO 63501-4221

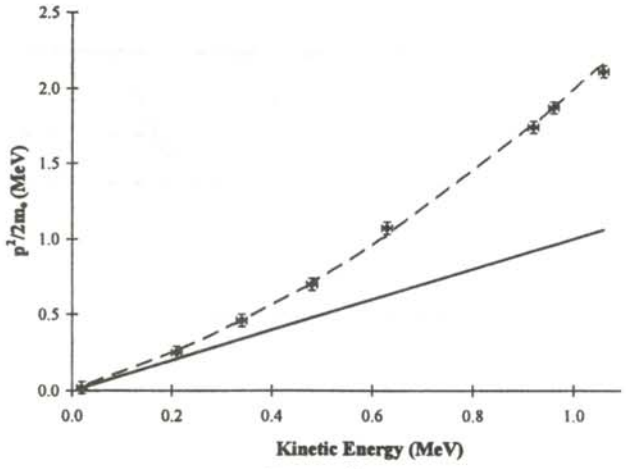

Figure 8
The classical and relativistic relationships between energy and momentum. The solid line represent the classical predictions, the dashed line the relativistic predictions.

SPIN DYNAMICS OF THE LAGEOS SATELLITE

Sukanya Chakrabarti *
Department of Mathematics
North Carolina State University
Raleigh, NC 27695-8205
received June 4, 1998

ABSTRACT

The Laser Geodynamic Satellite (LAGEOS) experiment is a proposed program to measure the relativistic Lense-Thirring precession as induced by the gravitomagnetic field of the earth. The Lense-Thirring precession of the orbit plane of the satellite is 0.031 arcsec/year. This relativistic effect is dwarfed by the classical contribution of the nodal precession of 126 degrees/year. To magnify the relativistic effect in comparison to the classical effect. It has been proposed to launch a second LAGEOS satellite into an orbit supplementary to LAGEOS I, i.e., if the orbit of LAGEOS I has inclination I, then that of the second LAGEOS-type satellite will have inclination π - I. For a paired satellite experiment, the classical effects will cancel, while the Lense-Thirring precession, or frame-dragging effect, will add. If perturbative effects can be accounted for adequately, an accurate measurement of the relativistic effect might be possible. Of the five dominant error sources in this experiment, the largest one involves surface forces, a function of the spin dynamics, on the satellite and the impact of these forces on the nodal precession. A previous analysis of the gravitational torques on the spin dynamics of a satellite suggested chaotic motion. In this paper we investigate the stability of the motion of the satellite. We derive the gravitational torques on the satellite. Numerical solutions for the precessional velocity show that it is bounded.

BACKGROUND

The first investigation into the nature of the gravitomagnetic field as a consequence of the general theory of relativity was made by Hans Thirring and Josef Lense. Their calculations evinced the structural analogy between the magnetic field produced by a dipole and the gravitomagnetic field produced by a massive spinning body. They found that in the weak field approximation the gravitational field of a rotating body is characterized by a "vector potential" that in the first approximation corresponds to the gravitational "magnetic" dipole due to the mass current. [1] We call this field the gravitomagnetic field. In the unit system where the gravitational constant $G = 1$ and the speed of light $c = 1$, this vector potential for a spinning mass M is given by:

$$\vec{G} \approx 2\,\frac{\vec{J}\times\vec{r}}{r^2}\,, \tag{1}$$

where J is the angular momentum and r is the distance from the center to the test mass.. Equation 1 is valid in the region where $r >> 2M$ and $r >> J/M$. The curl of the vector potential gives the gravitomagnetic field:

$$\nabla\times\vec{G} = \frac{J}{r^3}\left[3(\vec{r}\cdot\vec{J})\,\vec{r} - \vec{J}\right]. \tag{2}$$

This field would act on an orbiting gyroscope, producing a nodal precession at a rate given by:

$$\dot{\Omega}_{LT} = \frac{2J}{a^3\left(1-e^2\right)^{\frac{3}{2}}}\,, \tag{3}$$

where a is the size of the semimajor axis of the orbit, e is the eccentricity and Ω_{LT} is the longitude of the ascending node. This 'frame dragging' effect has been found to be a crucial ingredient in the dynamics of accretion disks, binary systems and other astrophysical phenomena. [2]

This 'frame dragging' or Lense-Thirring precession is so small for earth bound satellites that as of yet, it has not been experimentally verified. One of the most promising

Sukanya graduated from North Carolina State University summa cum laude with B.S. degrees in physics and philosophy. This research was begun during the summer of her junior year at Los Alamos national laboratory and continued during her senior year under the guidance of Dr. Arkady Kheyfets. She has also received the undergraduate research presentation award for her presentation of this work at the Undergraduate Research Colloquium at North Carolina State University. She is currently a first year graduate student at the Georgia Institute of Technology.

proposed experiments to detect this effect is the LAGEOS III approach. The LAGEOS is a dense, nearly spherical satellite, covered with laser reflectors in a medium altitude, high inclination orbit. Since the LAGEOS can be tracked very accurately with laser ranging, it can serve as an excellent measuring device to detect this 'frame-dragging' effect.

The orbital plane of the LAGEOS can be thought of as a gyroscope subject to the gravitomagnetic field. The Lense-Thirring precession of the orbit plane (nodal precession) amounts to about 0.031 arcsec/year. [3] This Lense-Thirring precession is very small compared to the classical precession and various other perturbations. The classical precession due to the oblateness of the satellite contributes 126 degrees/year to the total nodal precession.[4]

$$\dot{\Omega}_{measured} = \dot{\Omega}_{LT} + \dot{\Omega}_{classical} + \dot{\Omega}_{other}\,, \qquad (4)$$

where $\dot{\Omega}_{other}$ represents the precession due to perturbative forces.

The classical precession of a satellite $\dot{\Omega}_{classical}$ is modulated cos(I), where I is the inclination of the orbit. A scheme, shown in Figure 1, has been proposed to launch counter rotating satellite in supplementary orbits.[5] The classical effects on the precession cold be eliminated if the two measured precession rates, $\dot{\Omega}^{I}_{measured}$ and $\dot{\Omega}^{III}_{measured}$ are added together. Due to the change in sign of the cos(I) term, the classical precession terms would cancel while the relativistic effects would add. The Lense-Thirring precession rate would be:

$$2\,\dot{\Omega}_{LT} = \dot{\Omega}^{I}_{measured} + \dot{\Omega}^{III}_{measured} - \dot{\Omega}^{I+II}_{other}\,, \qquad (5)$$

where $\dot{\Omega}^{I+II}_{other}$ is the precession rate due to all other terms.

The viability of the experiment, therefore, hinges to a large extent on the ability to account for perturbative effects on the satellite. The dominant error source in this experiment

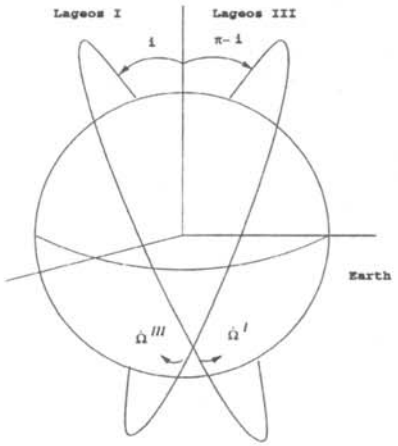

Figure 1
Proposed orbits of LAGEOSI and LAGEOS III satellites. The two orbits have supplementary inclination angles.

which can affect the nodal precession is due to surface forces on the satellite, such as Yarkowsky thermal drag or neutral and charged particle drag. [6]

Since the surface forces are a function of the spin dynamics of the satellite, so the behavior of the spin vector of the satellite, it is crucial to understand the behavior of the spin vector of the satellite in modeling the surface forces. In this paper, we develop a theoretical model of the spin dynamics of the satellite due to the gravitations torques and investigate the stability of the motion.

The prominent torque on the satellite is due to the gravitational field of the earth acting on the oblate satellite. Such torques arise when the satellite's bulging equatorial plane does not lie exactly in the plane of the orbit. We follow the development used by Goldstein [7] and consider the case of an oblate spheroid in orbit around a point mass.

Comments on Bertotti-Iess analysis

A previous analysis of the effects of gravity on the spin dynamics predicted chaotic motion. [8] This "Bertotti-Iess" analysis does not hold for small rate of spin, when the spin frequency approaches the orbital frequency in the asymptotic limit. Their analysis utilized the "Hipparcos" formula for the rate of precession, ω_p, of the oblate satellite in the gravity field of the earth: [9]

$$\omega_p = \frac{3}{2}\,\Delta\left(\frac{\omega_o^2}{\omega_3}\right)\cos(\theta)\,, \qquad (6)$$

where ω_o is the orbital angular velocity, ω_3 is the satellite spin rate, θ is the angle between ω_o and the normal to the orbital plan and $\Delta = I_3 - (I_1/I_2)$ is the oblateness of the satellite. I_1=I_2 are the principal moments of the satellite and I_3 is along the direction of ω_o which coincides with the symmetry axis of the satellite.

It was argued that since the rate of precession is inversely proportional to the satellite spin rate (when the spin rate approaches the orbital velocity), the gravitational precession would grow without bound, resulting in a chaotic spin dynamics. It has been shown[3] that even in the approximation used to derive Equation 6 (averaging the gravitational potential over the satellite orbit and cutting off the multipole decomposition at the dipole term), Equation 6 can only be used when:

$$6\,\Delta\left(\frac{\omega_o}{\omega_3}\cos(\theta)\right)^2 \approx \left(\frac{\omega_o}{\omega_3}\right)^2 << 1 \qquad (7)$$

or when the spin rate of the satellite is much greater than the orbital angular velocity. The expression for the precession frequency for comparable spin and orbital velocities is given by: [10]

$$\omega_p = \frac{\omega_3}{2}\cos(\theta)\left(1 - \sqrt{1 + 6\,\Delta\left(\frac{\omega_o}{\omega_3}\cos(\theta)\right)^2}\right). \qquad (8)$$

Equation 8 imposes a bound on the size of the precession frequency:

$$|\omega_p| < \omega_o \sqrt{\frac{3}{2}\Delta} \,. \tag{9}$$

Thus, the rate of precession cannot grow without bound to produce a chaotic spin dynamics.

GRAVITATIONAL TORQUES ON SATELLITE

The complexity of the analysis of the motion of spinning, orbiting bodies is largely due to the reference frames that must be invoked to describe the motion. We used an Earth Centered Inertial (ECI) reference frame. The ECI frame is fixed inertially in space with the origin at the center of the earth. The z_e axis is along the earth's rotational axis while the x_e and y_e axes lie in the equatorial plane. The x_e axis is in the direction of the Vernal Equinox. The standard Euler angles, shown in Figure 2, the nutation angle θ, the precession angle ϕ and the spin angle ψ are used to relate the body frame to our inertial coordinate system.

We obtain the gravitation equations of motion using the Lagrangian approach. The components of the moments of inertia are I_i. I_1=I_2 for our axially symmetric body. The components of the angular velocity vector, ω_i, are:

$$\begin{aligned} \omega_1 &= \dot{\phi}\sin(\theta)\sin(\psi) + \dot{\theta}\cos(\psi) \\ \omega_2 &= \dot{\phi}\sin(\theta)\cos(\psi) - \dot{\theta}\sin(\psi) \\ \omega_3 &= \dot{\phi}\cos(\theta) + \dot{\psi}\,, \end{aligned} \tag{10}$$

where the dots indicate derivatives with respect to time. The components of the torque, N_i, acting on the satellite are:

$$\begin{aligned} N_1 &= I_1\dot{\omega}_1 - (I_1 - I_3)\,\omega_2\omega_3 \\ N_2 &= I_1\dot{\omega}_2 - (I_1 - I_3)\,\omega_1\omega_3 \\ N_1 &= I_3\dot{\omega}_3\,. \end{aligned} \tag{11}$$

The Lagrangian function is:

$$L = T - V\,, \tag{12}$$

where T is the kinetic energy and V is the potential energy. The Lagrange equation of motion for a generalized coordinate q is:

$$\frac{d}{dt}\left(\frac{\partial L}{\partial \dot{q}}\right) - \frac{\partial L}{\partial q} = 0\,. \tag{13}$$

In our case, the generalized coordinates are the Euler angles.

The kinetic energy for our satellite is:

$$T = \frac{1}{2}\left[I_1\left(\omega_1^2 + \omega_2^2\right) + I_3\omega_3^2\right]\,. \tag{14}$$

Using Equations 10, the kinetic energy in terms of the Euler angles becomes:

$$T = \frac{1}{2}I_1\left(\dot{\phi}^2\sin^2(\theta) + \dot{\theta}^2\right) + \frac{1}{2}I_3\left(\dot{\phi}\cos(\theta) + \dot{\psi}\right)^2 \tag{15}$$

Solving the Lagrange equations for the three coordinates gives:

$$\begin{aligned} \ddot{\theta} &= -\frac{\dfrac{\partial V}{\partial \theta}}{I_1} \\ \ddot{\phi} &= -\frac{\dfrac{\partial V}{\partial \phi} + N_3\cos(\theta)}{I_1}\sin^2(\theta) \\ N_3 &= \frac{\partial V}{\partial \psi}\,. \end{aligned} \tag{16}$$

The gravitational potential for this system in the standard dipole approximations is:

$$V = \frac{G\,M(I_3 - I_1)}{2\,r^3}\left(3\gamma^2 - 1\right), \tag{17}$$

where γ is the direction cosine between the radial vector from the satellite center of mass to the center of the earth and the body axis, z_b, of the satellite. We can simplify the notation by letting:

$$\beta = \frac{3\,G\,M(I_3 - I_1)}{r^3}\,. \tag{18}$$

Equation 17 for the potential then becomes:

$$V = \frac{\beta}{6}\left(3\gamma^2 - 1\right). \tag{19}$$

The partial derivatives of the potential then take on the form:

$$\frac{\partial V}{\partial \theta} = \beta\,\gamma\frac{\partial \gamma}{\partial \theta}\,;\quad \frac{\partial V}{\partial \phi} = \beta\,\gamma\frac{\partial \gamma}{\partial \phi}\,;\quad \frac{\partial V}{\partial \psi} = \beta\,\gamma\frac{\partial \gamma}{\partial \psi}\,. \tag{20}$$

Expressing the direction cosine as:

$$\gamma = -\,\hat{r}\cdot\hat{z}_b \tag{21}$$

and the ECI coordinates of the unit vector along the body axis of the satellite in terms of the Euler angles, we get:

$$\left(\hat{z}_b\right)_e = \begin{pmatrix} \sin(\theta)\sin(\phi) \\ -\sin(\theta)\cos(\phi) \\ \cos(\theta) \end{pmatrix}. \tag{22}$$

The satellite position unit vector does not depend on the Euler angles, and may be represented as:

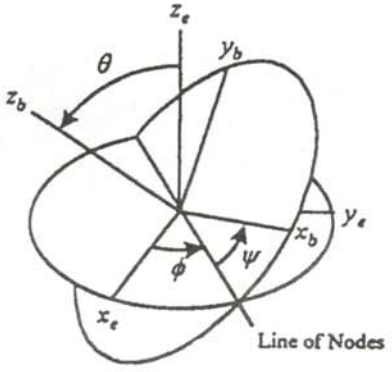

Figure 2
The Euler angles relating the earth centered inertial reference frame and the body frame of the satellite.

$$\hat{r}_e = \begin{pmatrix} \hat{r}_{xe} \\ \hat{r}_{ye} \\ \hat{r}_{ze} \end{pmatrix}. \quad (23)$$

Substituting Equations 22 and 23 into Equation 21 gives:

$$\gamma = -\left\{ \sin(\theta)\left[\hat{r}_{xe}\sin(\phi) - \hat{r}_{ye}\cos(\phi)\right] + \hat{r}_{ze}\cos(\theta) \right\} \quad (24)$$

Taking the derivative of γ in equation 24:

$$\frac{\partial\gamma}{\partial\theta} = -\left[\cos(\theta)\left(\hat{r}_{xe}\sin(\phi) - \hat{r}_{ye}\cos(\phi)\right) - \hat{r}_{ze}\sin(\theta)\right]$$
$$\frac{\partial\gamma}{\partial\phi} = -\sin(\theta)\left(\hat{r}_{xe}\cos(\phi) + \hat{r}_{ye}\sin(\phi)\right) \quad (25)$$
$$\frac{\partial\gamma}{\partial\psi} = 0 .$$

The equations of motion due to the gravitations torques become:

$$\ddot{\theta} = -\frac{\beta}{I_1}\gamma\frac{\partial\gamma}{\partial\theta}$$
$$\ddot{\phi} = -\frac{\beta}{I_1\sin^2(\theta)}\gamma\frac{\partial\gamma}{\partial\phi} \quad (26)$$
$$\ddot{\psi} = \frac{\beta\cos(\theta)}{I_1\sin^2(\theta)}\gamma\frac{\partial\gamma}{\partial\phi},$$

where β and g are given in Equations 18 and 24 and the partial derivatives of γ are in given in Equation 25.

RESULTS

Equations 26 are second-order, nonlinear differential equations free of singularities. The can be transformed to two sets of first order equations. There are many numerical methods for solving systems of first-order differential equations, such as Runge-Kutta, extrapolation and predictor-corrector methods. The Runge-Kutta method is often a default approach in computational science as it works well for a wide range of problems and is fairly simple to implement. For most well-conditions problems, however, extrapolation or predictor-corrector methods are actually more efficient. Thus, we chose the Burlisch-Stoer algorithm.[11] The model propagates the spin state of the satellite (Euler angles rates) over a period of one year. The data is output in the form of a state vector about once a day in the life of the satellite. The initial state vector is based on a known data point on July 29, 1992[12]. A run time of one year is sufficient as it was much greater than the three characteristic time periods involved in the motion of the satellite: the period of rotation; the period of the spin; the period of precession.

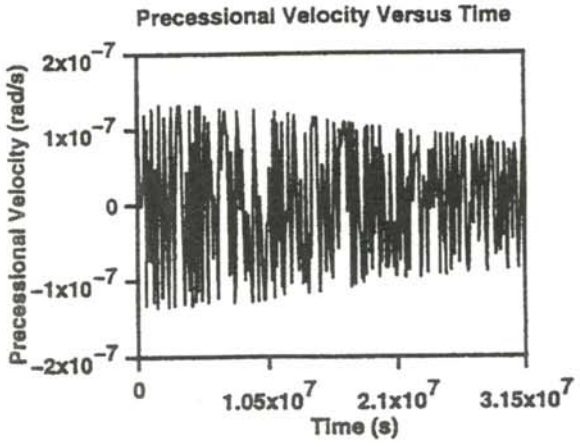

Figure 3
Results of the numerical integration of the equations of motion. This is a graph of the precessional velocity as a function of time. The precessional velocity remains bounded.

Our results are summarized in Figure 3. The numerical runs verify the theoretical bound on the precessional velocity. The value of $\dot{\phi}$ does not grow beyond its initial order of magnitude. The satellite does not experience chaotic motion.

This analysis of the contribution of the gravitational torques to the spin dynamics of the satellite was motivated by the hope that a predictable spin dynamics would allow for a measurement of the Lense-Thirring effect. However, magnetic torques and perturbative effects on the satellite must also be studied to comprehensively determine the spin dynamics of the satellite. The LAGEOS III approach, with its proposal for supplementary orbits to magnify the relativistic effect provides an optimal strategy for detecting the Lense-Thirring effect. As the gravitational torques on the satellite are the dominant torques, this analysis des suggest that the spin dynamics are stable. Work is currently underway to compare the observational data of the satellite with a more comprehensive model that includes the magnetic torques on the satellite.

ACKNOWLEDGMENTS

The author would like to thank Dr. Arkady Kheyfets for his sponsorship of this paper and for his support during the project.

REFERENCES

* Current address of the author: Department of Physics, Georgia Institute of Technology, 837 State Street, Atlanta, GA 30332-0430
1. H. Thirring and J. Lense, Phys.Z., 19, (1918), p. 156.
2. K.S. Thorne, R.H. Price, and Xia-He Zhang, Astrophysical Application of Black Hole Electrodynamics in Black Holes: The Membrane Paradigm, K.S. Thorne, R.H. Price and D.A. MacDonald, Eds. Yale University Press), 1986, Chapter 4.
3. A. Kheyfets, S. Habib, D.E. Holz, R.A. Matzner, W.A. Miller and B.W. Tolman, "Spin Dynamics of the LAGEOS Satellite in Support of a Measurement of the Earth's Gravitomagnetism", Phys.Rev. D., 50,10 (1994), p. 6068.

4. Ibid [3].
5. I. Ciufolini and J.A. Wheeler, Gravitation and Inertia, Princeton University Press, (1980), Chapter 6.
6. D.P. Rubincam, "Drag on the LAGEOS satellite, J. Geophys. Res., 95, (1990)
7. H. Goldstein, Classical Mechanics, Addison-Wesley Publishing, (1980), Chapter 5.
8. B. Bertotti and L. Iess, J. Geophys. Res., 96, (1991).
9. Ibid [9].
10. Ibid [3].
11. W.H. Press, S.A Teukolsky, W.T. Vetterline and B.P. Flannery, Numerical Recipes in FORTRAN, Cambridge University Press, (1992), Chapter 16.
12. S. Williams, "An Improved Model of the Spin dynamics of the LAGEOS Satellite", Master's Project Report at N.C. State University, December, 1997, (unpublished).

FACULTY SPONSOR

Dr. Arkady Kheyfets
Department of Mathematics
Box 8205
North Carolina State University
Raleigh, NC 27695-8205
Kheyfets@odin.math.ncsu.edu

DEVELOPMENT OF AN AUGER SPECTROMETER USING LOW-ENERGY ELECTRON DIFFRACTION OPTICS.

Ryan A. Munden *
Department of Physics
Stetson University
DeLand, FL 32720
received February 15, 1998

ABSTRACT

This paper reports on the adaptation of an existing low energy electron diffraction (LEED) system into an Auger spectrometer. Auger spectroscopy is an accurate method for analyzing the elemental composition of substances. High-energy incident electrons are shot at a sample freeing inner-shell electrons from the surface atoms. An outer-shell electron drops into the vacancy left by the ejected electron releasing excess energy. Instead of releasing the energy as a photon, it ejects a second electron. This Auger electron has an energy characteristic of the element. We constructed power supplies and configured the equipment to make a spectrometer capable of detecting submonolayer amounts of carbon. With this system, Auger spectroscopy can be performed on the same sample as LEED without having to remove the sample from the ultrahigh vacuum chamber.

INTRODUCTION

Auger electron spectroscopy (AES) is a method of determining the elemental composition of surfaces by the analysis of the energies of Auger electrons. [1-4] The process for releasing Auger electrons begins when an incident electron from an high energy electron beam collides with an inner shell electron in one of the atoms in the sample. The inner shell electron (e.g. an *L* level electron) is knocked free leaving an energy vacancy. An outer shell electron (e.g. an *M* level electron) in the atom then fills the vacancy due to the ejection of the *L* electron. The energy is released by ejecting a second outer electron (e.g. another *M* level electron). This ejected second outer shell electron is the Auger electron. Since the energy of the atom is quantized, the Auger electron is released with a specific amount of kinetic energy that is characteristic of the atom which ejected the Auger electron. This process, a

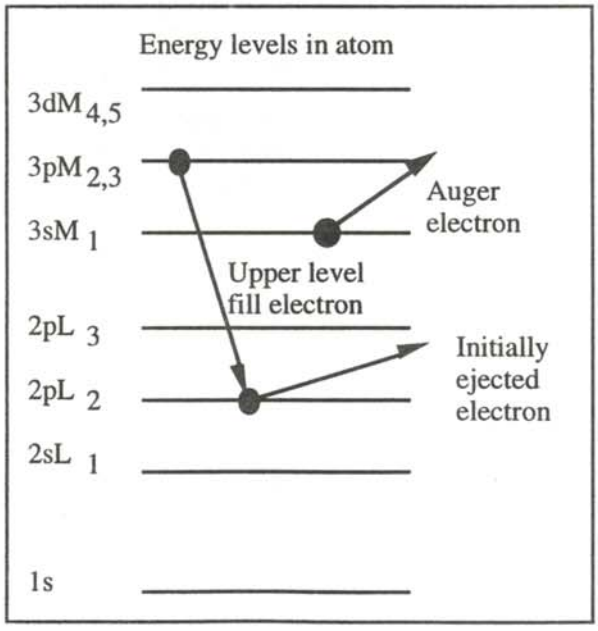

Figure 1
Schematic diagram of an LMM Auger process.

Ryan is a junior physics major at Stetson University. He wrote a grant application for this project and it was funded by Stetson University's Summer Undergraduate Research Experience program. The research was performed during the summer of 1997. He presented the results of this research in a talk at the student section of the 1997 Southeastern Section of the American Physical Society meeting. He was co-winner of the Marsh W. White Award for the best undergraduate research paper.

Ryan is currently taking time off from his studies to work for his church as a missionary in Mexico. He will return to Stetson University in the spring of 2000. After completing this undergraduate degree, he plans to pursue an advanced degree in physics. He has not yet decided on an area of specialization.

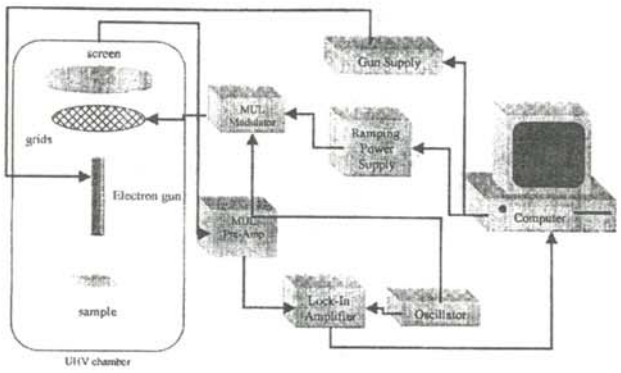

Figure 2
Block diagram of the Auger spectrometer.

LMM transition, is schematically shown in Figure 1. Other transitions, such as *KLL* or *MNN* produce Auger electrons. The Auger process is similar to what happens when x-ray photons are ejected to carry away the excess energy when high energy electrons drive out inner shell electrons. Instead of finding the wavelength of the emitted x-rays, the energy of the Auger electrons can be used to determine what type of atoms are releasing the electrons.

Unlike x-ray production, AES is surface sensitive. The bombarding electrons may penetrate deep into the sample, but the lower energy Auger electrons have a limited escape depth. Only Auger electrons released within the atomic layers near the surface are able to escape the sample without losing most of their kinetic energy due to collisions.

DEVELOPING THE SPECTROMETER

We had a ultra high vacuum (UHV) system to perform low energy electron diffraction (LEED). [5] We could improve the results of the LEED if we were able to perform AES on the sample first to determine how clean the sample was without removing it from the vacuum chamber. We converted the existing equipment by building our own power supplies, using the LEED electron gun supply and developing our own data collection techniques and software to run the experiment and interpret the data.

Figure 2 shows a block diagram of our apparatus. The gun supply was set to produce electrons at approximately three times the energy of the Auger peak for which we were scanning. The electrons from the gun bombard the sample, causing the surface of the sample to eject Auger electrons. The Auger electrons pass through the grids to be collected on the screen. A retarding potential was applied to the grids. Only electrons with energy greater than the retarding voltage were collected on the screen. The retarding potential was varied under computer control and was oscillated by the internal oscillator of the lock-in amplifier. The current of electrons collected on the screen went through a preamplifier [6] to the lock-in amplifier to be analyzed and sent to the computer.

A programmable high voltage supply provided the retarding voltage applied between the sample and the grid.[7] The output of that supply was controlled by the combination of an input voltage and the choice of a resistance. Changing the size of the resistance changed the range of the scan voltage. The input voltage consisted of the sum of the voltages from a second voltage supply [8] and the output of the digital-to-analog converter (DAC) from the computer. The second voltage supply controlled the initial starting point for the scan and the DAC controlled the range and rate of the voltage ramp.

We used a lock-in amplifier to separate the desired signal from the background noise. The retarding voltage applied to the grids was oscillated at the reference frequency of the lock-in amplifier. Thus, only the signal that came from the electrons that passed through the grids was detected by the lock-in amplifier. The lock-in amplifier also allowed us to take readings of the first and second derivatives with respect to energy of the current signal by taking data at the first and second harmonics of the reference frequency. The first harmonic signal analysis would give a plot of $N(E)$, the number of Auger electrons as a function of energy. The second harmonic signal analysis gives dN/dE as a function of the energy of the collected Auger electron.

To match the signal from the lock-in amplifier to the computer's 12 bit analog-to-digital input, a circuit had to be built to convert the bipolar 12 V lock-in output signal to a unipolar 0 - 10 V signal. The circuit diagram for this is shown in Figure 3.

SIGNAL ANALYSIS

Figure 4 shows the possible ways to process the signal from the Auger spectrometer. In this case, we examined the electrons produced when electrons with an energy of 150 eV were shot at the sample. Figure 4a shows a reconstruction of the actual electron current as it entered the lock-in amplifier as a function of the retarding voltage applied to the grid. Thus, Figure 4a shows the number of all electrons ejected from the sample with enough energy to pass through the retarding grid ($E_{electron} > e\,V_{retard}$) as a function of retarding voltage.

Figure 4b shows a first harmonic scan of this signal: the number of electrons as a function of energy. The peak at

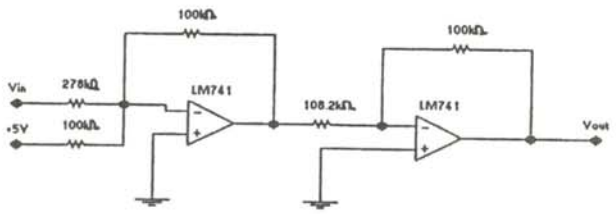

Figure 3
Diagram of the circuit used to condition the output of the lock-in amplifier for input into the computer A/D card.

150 eV consists of electrons that scattered elastically from the sample. Figure 4c shows the second harmonic scan: d*N*/d*E* as a function of energy. Auger spectroscopy is most often performed using d*N*/d*E* scans because slowly varying changes in the number of electrons as a function of energy are suppressed. Rapid changes show up as a bipolar peak that is easy to identify, even when the peak is small. The crossover point in the bipolar peak in Figure 4c is at 150 eV, corresponding to the maximum of the peak shown in Figure 4b.

To test our spectrometer, we used a pure silicon crystal, which produces a 92 eV Auger electron. We collected data using the second harmonic scanning mode. Figure 5 is a plot of the second harmonic signal (dN/dE) as a function of the energy of the ejected Auger electrons. The data shown in Figure 5 was collected with an 5 μA incident electron beam at 500 eV and a 1.0 V_{rms} modulation on the retarding grid. The scan shows ejected electrons in the 50 - 150 eV range. Figure 5 shows a clear peak near 92 eV. There is also a small second peak noticeable near 72 eV. This is the expected Auger spectrum for silicon. These results gave us confidence that our system was working properly.

Since the silicon crystal was somewhat abused by all our testing, we attempted to look for contamination of the sample. We expected that there should be some residual methane that the UHV system could not pump out. The electron beam bombarding the sample encourages the methane to ionize and carbon to bond to the surface of the sample, causing a high likelihood of carbon contamination of the sample. Carbon produces a 280 eV Auger electron. Figure 6 shows the data for a second harmonic scan in the energy range 250 - 350 eV with an 8.5 μA, 570 eV incident beam and 5.0 V_{rms} modulation on the retarding grid. The sensitivity of the lock-in amplifier was turned up by a factor of 10 compared to the scan in Figure 5. A peak at 280 eV is clearly evident showing that our sample has a small surface contamination of carbon.

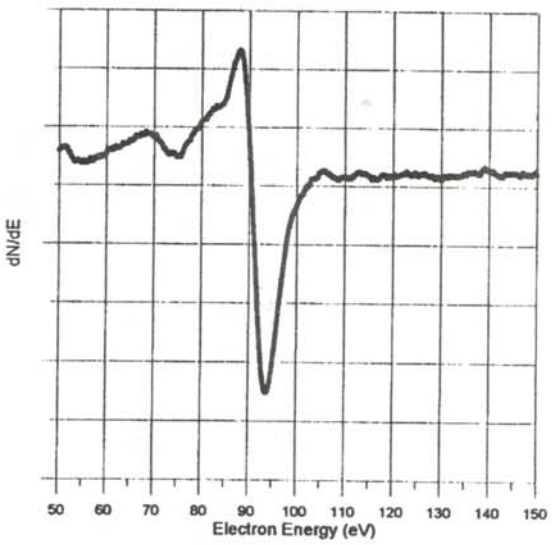

Figure 5
Auger spectrum obtained from a silicon crystal. The second harmonic scan shows 92 eV (and smaller 72 eV peak) obtained with a 5 μA incident electron beam at 500 eV and a 1.0 V_{rms} modulation on the retarding grid.

ACKNOWLEDGMENTS
The author would like to thank Dr. Glander for his guidance and assistance at every stage of this project. He acknowledges the many things taught to him during this

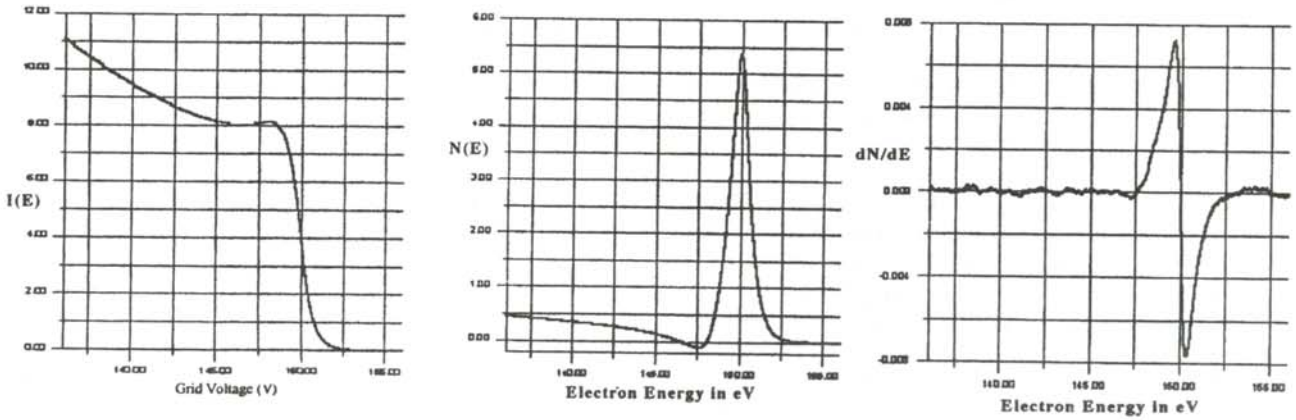

(a) *(b)* *(c)*

Figure 4
Examples of signal processing techniques. The scan is set to look at the elastically scattered electrons. a) electron current as a function of grid voltage; b) the number of electrons as a function of energy (first harmonic measurement by the lock-in amplifier; c) dN/dE as a function of energy (the second harmonic measurement by the lock-in amplifier.

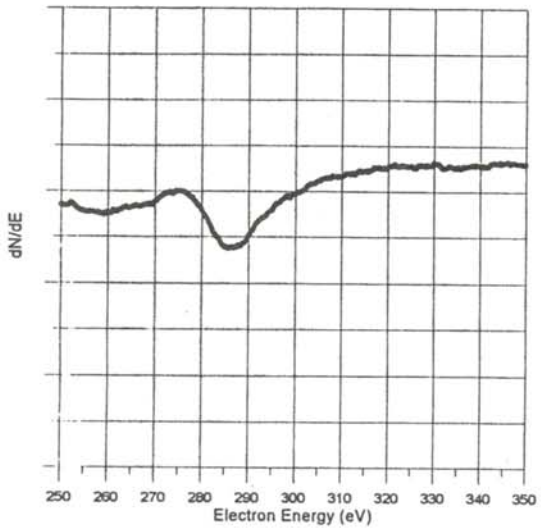

Figure 6
Auger spectrum searching for impurities in a silicon crystal. The second harmonic scan shows the 270 eV carbon Auger peak obtained with an 8.5 μA incident electron beam at 570 eV with a 5.0 V_{rms} modulation on the retarding grid.

project. The author would like to thank Stetson University for its financial support of this project by awarding the author a Summer Undergraduate Research Experience grant and providing the author's mentor with a Summer Research grant.

REFERENCES

* Current address of author: Ryan Munden, c/o Physics Department, Stetson University, 421 N. Woodland Blvd., Unit 8267, DeLand, FL 32720
1. "Auger Effect", McGraw-Hill Encyclopedia of Science and Technology, 7th Ed. Vol 2, (McGraw-Hill, 1992) p. 272
2. L.E. Davis, N.C. MacDonald, P.W. Palmberg, G.E. Riach and R.E. Weber, Handbook of Auger Electron Spectroscopy, 2nd Ed., Physical Electronics Division, Perkin-Elmer Crop, 1976.
3. A.W. Czanderna, Ed. Methods of Surface Analysis, (Elsevier, New York, 1975).
4. Charles, Evans and Assoc. "Auger Electron Spectrometry Theory Tutorial", http://www.cea.com/cai.augther/caiatheo.htm.
5. The LEED optics are a commercial 4-grid, rear-view system manufactured by Omicron. The electron gun, retarding grids and screen are controlled by Omicron's NGL10 Spectraleed Control Unit.
6. We purchased the cable and preamp that Omicron sells for their Auger spectroscopy control unit. We rewired the connector so that it could be used with the NGL10 control unit to run the electron gun. The cable and preamp had terminals for inputting the retarding voltage, modulation voltage and screen bias, and for outputting the signal. We had to build voltage supplies for the preamp and screen bias. By switching between the standard LEED cable and the modified cable, we could switch between LEED and Auger spectroscopy.
7. We used a Kepco OPS-2000 high voltage operational power supply. It was used in the same way as an op-amp, but delivers voltages in the range 0 - 2000V.
8. We used an Enco Model XP-620 regulated power supply to provide voltages in the range 0 - 30V.

FACULTY SPONSOR

Professor George S. Glander
Department of Physics
Stetson University
DeLand, FL 32720-3756
physics@stetson.edu

SHOE-STRING INTERFEROMETRY

Jenny Flood *, Ryan Scheetz § and Marta Sieradzan †
Department of Physics
Central Michigan University
Mt. Pleasant, MI 48859
received July 16, 1998

ABSTRACT

Enormous light intensities can be obtained in a high finesse Fabry-Perot interferometer cavity when it is illuminated by a well collimated beam and tuned for maximum transmission. To demonstrate this interesting effect in a classroom environment , we developed a mechanical shoe-string Fabry-Perot interferometer that uses a string vibrator and fishing weights. We also present a theoretical model for this interferometer. The shoe-string interferometer shows a build up on energy in the cavity that is consistent with our theoretical model.

INTRODUCTION

Fabry-Perot Interferometer

Since its invention almost 100 years ago, the Fabry-Perot (F-P) interferometer has been among the most important tools of high-resolution spectroscopy. This device consists primarily of two semitransparent mirrors aligned parallel to each other. This system is a tunable spectral filter. Derivation of the F-P transmission intensity, I_t, is an excellent example of light interference principles and can be found in every textbook on wave optics. [1]

$$I_t = \frac{I_o T^2}{1 - 2R\cos\left(\frac{4\pi d\cos(\theta)}{\lambda}\right) + R^2}, \qquad (1)$$

Where I_o is the incident beam intensity, d is the distance between the mirrors, θ the angle of incidence of the light, λ the wavelength of the light, T the transmission coefficient of an individual mirror and R the reflection coefficient of an individual mirror. For ideal lossless mirrors:

$$R + T = 1 . \qquad (2)$$

Figure 1 shows the corresponding transmission curves from Equation 1 for 4 different R values for the mirrors. Note that 100% transmission ($I_t = I_o$) is reached every time the 'resonance condition'

$$2\,d\cos(\theta) = m\,\lambda \quad (m = 1, 2, \ldots) \qquad (3)$$

is satisfied. This property is independent of the reflectivity of the mirrors, it even works for practically non-transmitting mirrors where $R \approx 1$. In such cases, the transmission

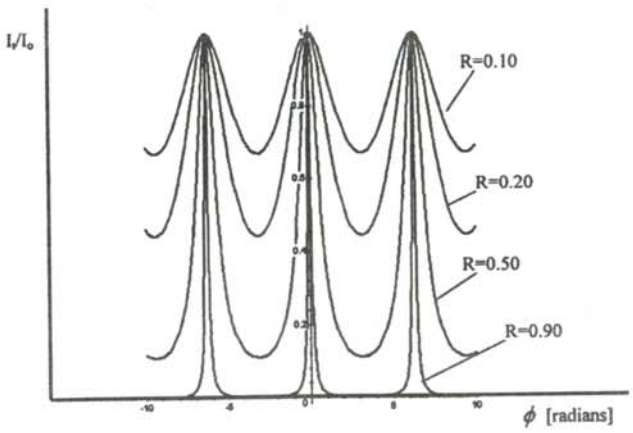

Figure 1
A representative set of transmissions curves as a function of ϕ, the phase shift acquired by the beam on a round trip between the reflectors.

Ryan is a senior mathematics major and physics minor at Central Michigan University. He plans to graduate in December of 1999 after he finishes his student teaching. In his spare time, Ryan enjoys mountain biking and water skiing.

Jenny finished student teaching and earned a Bachelor's degree with a major in mathematics and a minor in physics in December of 1998. She also became a newlywed in December. She currently is enjoying spending time with her husband and is looking forward to starting a career in education.

Marta is an Engineering major at the University of Michigan, planning to graduate in December of 1999. She worked on this project during her summer visit to her hometown. In her spare time, Marta enjoys traveling to distant places.

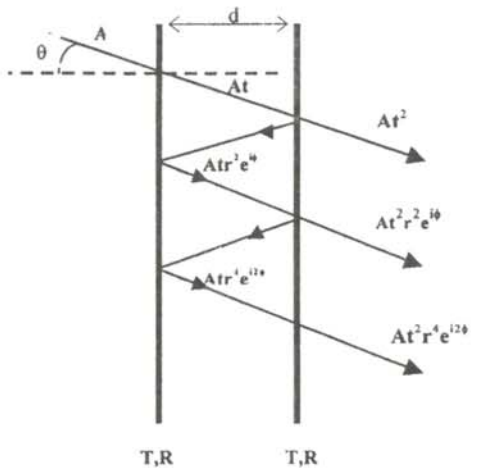

Figure 2
Schematic diagram of a Fabry Perot interferometer showing reflected and transmitted waves.

peaks become very narrow, but total transparency is still taking place at selected wavelengths and mirror separations.

Inside the F-P Cavity

An aspect of the F-P interferometer that has not always been appreciated (we found no textbook treatment of the subject) is its ability to store optical energy and 'produce' high light intensity inside the cavity. This phenomenon is interesting as its analysis is helpful in learning about energy redistribution in the interference context and because the high intracavity power has begun to be utilized in physics laboratories. [2]

Consider a F-P interferometer (see Figure 2) made of a pair of lossless $R = 0.9998$ reflectors. Assume that there is a perfectly parallel alignment and a wide incident beam. The complex amplitudes of the waves contributing to the net intracavity wave moving to the right are:

$$A\,t\,;\,A\,t\,r^2\,e^{i\phi}\,;\,A\,t\,r^4\,e^{i2\phi},\,\ldots \qquad (4)$$

where A is the amplitude of the incident wave, $t = \sqrt{T}$ the transmission coefficient for the amplitude and $r = \sqrt{R}$ the amplitude reflection coefficient. For waves traveling to the left:

$$A\,t\,r\,;\,A\,t\,r^3\,e^{i\phi}\,;\,A\,t\,r^5\,e^{i2\phi}\,;\,\ldots \qquad (5)$$

where ϕ, the phase shift between consecutive transmitted or reflected light waves, is:

$$\phi = \frac{4\pi d\cos(\theta)}{\lambda}\,. \qquad (6)$$

The net amplitudes and hence the intensities of the waves moving to the left, I_l, and right, I_r, can be found using an infinite geometric series. The total intracavity average intensity, I_c, obtained is:

$$I_c = I_r + I_l = \frac{(R+1)}{T}\,I_t\,, \qquad (7)$$

where I_t is given in Equation 1.

The actual value of I_c depends on the phase angle ϕ, but at resonance it reaches $9999I_o$ for mirrors with $R = 0$ .9998. This value makes good sense. If I_o is the exiting beam intensity, then the wave incident from the left on the exit mirror must have an intensity of $5000I_o$ since a single mirror is a very simple device; $R = 0.9998$ means that only 0.0002 of the total incident intensity goes through, so the incident beam is 5000 times more intense. In the steady state, with $5000I_o$ reaching the exit mirror, a wave of intensity $4999I_o$ must continuously turn back to the left. This gives a total of $9999I_o$ average intracavity intensity.

The extremely high intensities predicted by our treatment may be hard to obtain in practice. These results only hold for a truly lossless interferometer. A more realistic treatment must include the ever present losses due to light diffraction, absorption in the reflectors and the medium between them. We introduce losses into our calculations by multiplying the wave amplitude by a factor (<1) every time the light travels between the reflectors. Although the exact nature of the losses and the relative importance of different contributing factors are not specified, the treatment reflects well the anticipated effect of losing energy from the beam. Results of these calculations are shown in Figure 3.

Demonstrating Intracavity Intensity

The intracavity energy buildup as described above has been observed experimentally. [2] However, mirrors of the required quality and a laser and electronics good enough to keep the interferometer steadily in resonance are forbiddingly expensive. Therefore, we asked ourselves if it would be possible to demonstrate these effects with

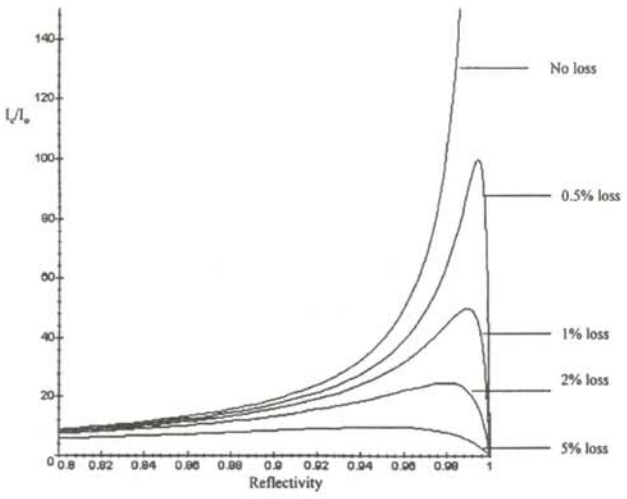

Figure 3
Intracavity intensity buildup, I_c/I_o, as a function of the mirror reflectivity, R. Different curves correspond to different levels of losses, defined as the percentage amplitude loss on a single pass through the cavity.

equipment that is inexpensive and readily available. We decided to build an interferometer using waves on a spring driven by a mechanical shaker. The first idea was to make a string that had a piece of different mass/length in the middle. Although this arrangement is similar to a solid Fabry-Perot etalon that has different wave speed between reflecting surfaces, it did not work well. A better F-P string interferometer can be made by attaching small masses to the string as partial reflectors. No reflection would occur if the mass were zero, 100% reflection would occur in the high-mass limit. The point where the mass was attached would behave like a partial reflector for intermediate masses. One can find more discussions of 'beaded strings' elsewhere. [3,4]

ANALYSIS OF THE STRING INTERFEROMETER

The behavior of this string interferometer is done by examining the boundary conditions for the waves at each of the masses. We start by finding the transmission coefficient for the interferometer that has a section length L of different mass/length (μ) string in the middle. To make this section appear later as a point mass, we must shrink L while keeping $L\mu = m$ constant.

We model the string interferometer as shown in Figure 4. In analogy to the quantum mechanical potential barrier problem [5], the waves functions, excluding the common time dependence factor $e^{-i\omega t}$, in the three regions shown in Figure 4 are:

$$\begin{aligned} \varphi_I &= A\, e^{ik_1 x} + B\, e^{-ik_1 x} \\ \varphi_{II} &= C\, e^{ik_2 x} + D\, e^{-ik_2 x} \\ \varphi_{III} &= G\, e^{ik_1 x} + H\, e^{-ik_1 x} \end{aligned} \tag{8}$$

where

$$\begin{aligned} k_1 &= \frac{2\pi}{\lambda_1} = \frac{2\pi\nu}{\sqrt{\frac{F}{\mu_1}}} \\ k_2 &= \frac{2\pi}{\lambda_2} = \frac{2\pi\nu}{\sqrt{\frac{F}{\mu_2}}} \end{aligned} \tag{9}$$

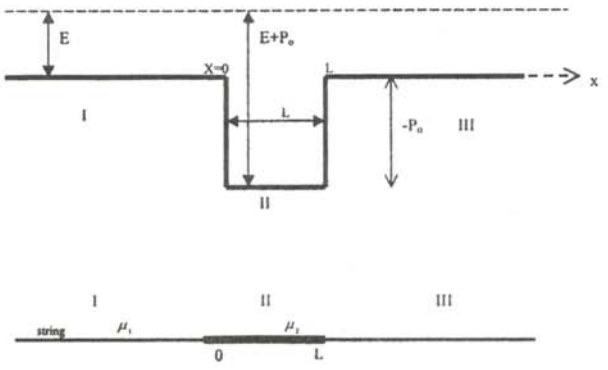

Figure 4

Fabry-Perot etalon mechanical set-up with a piece of string of different mass/length inserted and the equivalent potential problem.

and F is the tension in the string, μ_1 the mass/length of the original string and μ_2 the mass/length of the middle section of string. The boundary conditions are that at the joints, the string must be continuous and that the first derivative of the wave functions be continuous. These conditions, together with the requirement that no returning wave comes from region III (see Figure 4) give rise to:

$$\begin{aligned} H &= 0 \\ A + B &= C + D \\ k_1 A - k_1 B &= k_2 C - k_2 D \\ C\, e^{ik_2 L} + D\, e^{-ik_2 L} &= G\, e^{ik_1 L} \\ i k_2 C\, e^{ik_2 L} - i k_2 D\, e^{ik_2 L} &= i k_1 G\, e^{ik_1 L} \end{aligned} \tag{10}$$

From Equation 10, we find that:

$$A = G\, e^{ik_1 L}\left[\cos(k_2 L) - \frac{i}{2}\left(\frac{k_1}{k_2} + \frac{k_2}{k_1}\right)\sin(k_2 L)\right]. \tag{11}$$

Since $|A|^2$ is the intensity of the incident wave and $|G|^2$ is the intensity of the transmitted wave, the transmission coefficient is:

$$T = \frac{I_T}{I_o} = \frac{|G|^2}{|A|^2} = \left[1 + \frac{1}{4}\left(\frac{k_1}{k_2} - \frac{k_2}{k_1}\right)^2 \sin^2(k_2 L)\right]^{-1}. \tag{12}$$

When Equation 9 is substituted into Equation 12, we find that:

$$T = \left[1 + \frac{1}{4}\left(\frac{\sqrt{\mu_2}}{\sqrt{\mu_1}} - \frac{\sqrt{\mu_1}}{\sqrt{\mu_2}}\right)^2 \sin^2\left(\frac{2\pi\nu\sqrt{\mu_2}\,L}{\sqrt{F}}\right)\right]^{-1}. \tag{13}$$

Now taking the limit as L gets small, while keeping $L\mu_2 = m$ constant, Equation 13 becomes:

$$T = \frac{F\mu_1}{\pi^2\nu^2 m^2 + F\mu_1} \tag{14}$$

where m is the mass attached to the string. As the extra mass goes to zero, the transmission reaches 100%. As the extra mass approaches infinity, the transmission goes to zero.

Figure 5

Demonstration of the mirrorlike behavior of a small mass attached to the strong. Note that a standing wave forms between the end of the string and the point mass.

Determining Phases

To characterize the wave reflector completely, we must specify not only the intensity of the transmitted/reflected wave, but also its phase relative to the phase of the incident wave. Notice that Equation 11 is a simple proportionality. If the proportionality factor were real, the phases of the incident wave and the transmitted wave would be identical. Since the proportionality factor is complex, these two waves are generally phase-shifted. From Equation 11 we get in the limiting case for a point mass:

$$G = A \frac{1 + \frac{i}{2}\frac{k_2^{\,2}}{k_1} L}{1 + \frac{1}{4}\frac{k_2^{\,4}}{k_1^{\,2}} L}. \qquad (15)$$

From Equation 15 we find that the transmitted wave (G) is phase shifted with respect to the incident wave, (A) by an angle α, where:

$$\tan(\alpha) = \frac{k_2^{\,2} L}{2 k_1} = \frac{\pi \nu}{\sqrt{F \mu_1}} m. \qquad (16)$$

When m is very small and reflection is weak, the transmitted wave has the original wave phase. For substantial m, or when the reflection is high, the transmitted wave acquires a phase shift of almost 90°.

To find the phase of the reflected wave, B, we used the simplified boundary condition:

$$\varphi_I = \varphi_{III} \text{ at } x = 0 \text{ or } A + B = G \qquad (17)$$

Using Equation 15, and solving Equation 17 for B gives:

$$B = G - G\left(1 - \frac{i}{2}\frac{k_2^{\,2}}{k_1} L\right) = i\left(G \frac{k_2^{\,2}}{2 k_1} L\right). \qquad (18)$$

The proportionality factor between B and G is imaginary, so the phase shift between reflected and transmitted wave, β, is always 90° and is independent of the mass.

To determine the phase relation between the incident wave and the reflected wave, we must add α and β. The reflected wave is shifted by 90° with respect to the incident wave when $m \to 0$. This is initially alarming, but is cleared by recognizing that at the same time, the reflected wave amplitude vanishes. For a substantial m, the reflected/transmitted phase difference reaches 180° (opposite phase) when R is close to 1. This resembles the behavior of highly reflective optical mirrors.

THE EXPERIMENT

To demonstrate the string interferometer, we used a stretched wire that passes through the gap of a magnet. When an alternating current from a function generator is sent through the wire, the wire is driven up and down by the Lorentz force. Small fishing line sinkers from a set containing different sizes were used as the masses that define the F-P interferometer cavity. Choosing the correct mass of the 'reflector' is a crucial part of the demonstration since the intracavity intensity is highly dependent upon loss factors and the transmission coefficient of the 'reflectors'.

The first demonstration uses a single mass attached to the wire. If the tension, frequency and distance to the mass are adjusted to resonance, a standing wave is created between the end of the string closer to the source and the attached mass. As seen in Figure 5, there is no noticeable transmitted wave. This displays the mirrorlike properties of a point mass.

In the next demonstration, a second identical mass is placed on the string, creating a true mechanical analog to the Fabry-Perot interferometer. Varying the mass, the placement of the masses on the string and the frequency of the wave, we obtained a strong standing wave within the cavity with no visible wave outside the cavity as shown in Figures 6 and 7. Most of the energy is not in the vicinity of the sources, but trapped inside the cavity. The maximum intracavity intensity was observed with $F = 4.0$ N, μ_1

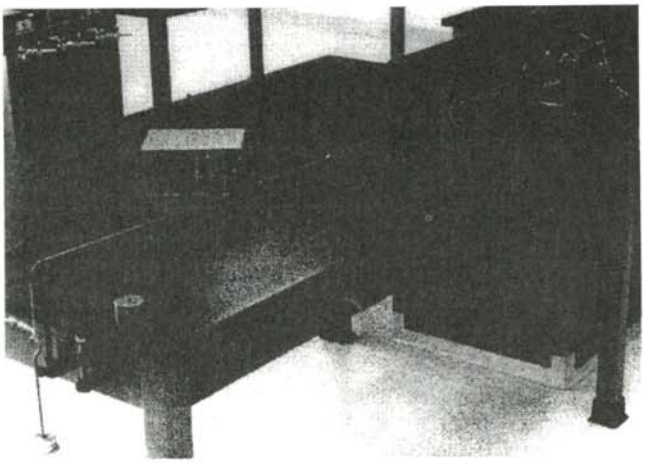

Figure 6
Mechanical model of the Fabry-Perot interferometer. a) general view,

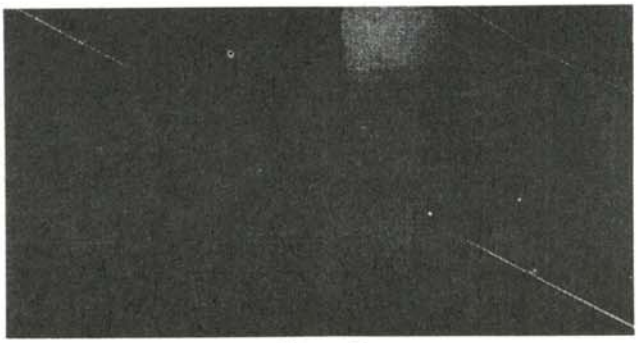

Figure 7
A close-up view of the central portion of the string interferometer. Intracavity power build-up is evident.

= 3.08 gm/m, ϖ = 43.72 Hz, and mass m of each of the 'reflectors' = 7 gm.

Substituting these values into Equation 14, we get a transmission coefficient of $T = 0.016$. Assuming no loss, the reflection coefficient $R = 0.994$. Using 'eye ball' measurements, we estimated the amplitude ratio between the intracavity wave and the incident wave to be between 10 and 20. This gives an intracavity intensity increase between 100 and 400. From the graph shown in Figure 3, we found that to obtain such an intracavity intensity increase, one needs a reflectivity coefficient of approximately 0.995, consistent with our calculated reflection coefficient.

This is a simple and effective demonstration of the energy trapping characteristic of the Fabry-Perot cavity. The point masses act as partially reflecting mirrors. The string interferometer displays the intracavity intensity increase at resonance. The simple wave model of this system models the experiment well.

ACKNOWLEDGMENTS

The authors would like to thank to Central Michigan University for financial support for this work. Jenny Flood was sponsored with the CMU Office of Research Summer Scholar program and Ryan Scheetz with the faculty advisor's research grant.

REFERENCES

* Current address of author: R. Scheetz: Physics Department, Central Michigan University, Mt. Pleasant, MI.
§ Current address of author: M. Sieradzan: School of Engineering, University of Michigan, Ann Arbor, MI
† Current address of author: J. Flood: 1500 Rose St. Apt#2, Bay City, MI 48708.

1. See, for example, F. Pedrotti and L. Pedrotti, Introduction to Optics, 2nd Ed., (Prentice-Hall), 1993, pp,. 233-239.
2. C.S. Wood, et al., "Measurement of Parity Nonconservation and an Anapole Moment in Cesium", Science, 275, (March 21, 1997), pp. 1759-1763.
3. S. Pamley, et al., "Vibrational Properties of a Loaded String", Am J. Phys., 63, (June 1995), pp. 547-553.
4. P. Allen and J. Kelner, "Evolution of a Vibrational Wave Packet on a Disordered Chain", Am. J. Phys., 66,

STOCHASTIC TRANSPORT AND ACCELERATION OF SOLAR FLARE ELECTRONS

M.L. Edwards *
Physics Department
Roanoke College
Salem, VA 24153
received May 21, 1998

ABSTRACT

We studied numerically the transport, energy loss due to synchrotron radiation, inverse Compton scattering and adiabatic deceleration and the energy gain due to diffusive and shock accelerations of solar flare electrons. We solved the transport equation in time, space and momentum variables using the numerical method of lines with an implicit integration routine. Steady state solutions of the transport equation are compared to satellite observations of solar flare electrons in the energy range of thermal to relativistic electron energies. In both calculation and observation, a two index power law spectrum is seen for the electrons, with a clear break in the kinetic energy at 100-200 keV. While this break in the spectral index has been attributed to two acceleration mechanisms, in this study we show that a second order Fermi mechanism at the flare site can describe the electron data if the break is attributed to the accelerating efficiency of the flare itself.

INTRODUCTION

To space physicists interested in the transport of energetic charged particles, the solar system presents a unique *in situ* laboratory where direct observations of such particles can be made either near the earth, in deep space or over the solar poles. In such environments, a wide range of particle species and energies can be detected by instruments on board satellites and spacecraft. These measurements are often collected in real time. Shock waves, whether at the sun, in the sun, in the earth's magnetosphere, or at the edge of the solar system, are known to be powerful accelerators of energetic particles. In the heliosphere, a solar flare and its associated shock waves easily can accelerate particles to suprathermal energies. Unlike our cleanly controlled ground based particle accelerators, we do not have control of either the method or the types of particles accelerated in these natural accelerators.

Michael Edwards is a first year Master student at the University of Denver in the Department of Physics and Astronomy. This research was begun when he was a junior physics and math major at Roanoke College. This paper won Roanoke College's 1997-98 Guy Echman Award for best student research paper. In his spare time, he can be found on line MUDing or adding to his collection of classic science fiction novels.

Because of the inherently passive nature of measurements of the output of these natural accelerators, models of both acceleration and transport mechanisms have to be developed before any meaningful interpretation of the collected data can be made. Many studies have suggested that there are several, perhaps distinct, acceleration processes at work in a single solar flare. [1-6] Even in the impulsive or flash phase of rather small flares, electrons can be accelerated to suprathermal energies of between 10 and 100 keV by transferring stored magnetic energy to the electrons via a magnetohydrodynamic interaction. A second acceleration method closely associated with shock waves in the solar atmosphere is thought to be able to accelerate particles to MeV energies and higher.

A study of wide energy range (20 keV - 20 MeV) electron data was conducted using data from the near earth satellites IMP 6, 7 and 8. [6] Care was taken to minimize the effect of interplanetary contamination such as from Jovian electrons. This study fit the electron spectrum above 100 keV with two power laws, one between 100 keV and 1 MeV and a second for the data above 1 MeV. The study suggested that these two power laws indicated the presence of two distinct acceleration mechanisms taking place. The data showed that this break in the energy spectrum did not seem to change in any appreciable way from flare to flare. The authors suggest that a single high energy acceleration phase may dominate while the other phase may act as an injection source of lower energy electrons to the high energy phase. Correlations of the electron data

with radio, x-ray and gamma ray observations of the same events were consistent with acceleration by the flare shock wave as it passes the solar corona.

Recent theoretical discoveries in the acceleration and transport of charged particles in space and astrophysical plasmas suggest that both of the processes discussed are diffusive in nature. [7] If so, both the acceleration and transport processes are not expected to retain any memory of contributing mechanisms because all diffusion processes are memory-less stochastic processes. [8] In steady-state conditions, one is essentially sampling one or an incoherent sum of a number of processes. The distinction between an average process and a true single process is inherently blurred. In transient time-sensitive conditions, the distinction is in principle manifested if the physical parameters of the contributing mechanisms are both time-sensitive and act over vastly different time scales. Consequently, the modeling of solar flare events without this aspect of the flare acceleration mechanisms is not expected to be able to make any such distinctions.

THEORY OF STOCHASTIC TRANSPORT AND ACCELERATION

The transport theory of energetic charged particles in the heliosphere is essentially a statistical description of the motion of the particle using the evolution of its phase-space or number density functions in space and time, subjected to the appropriate conservation laws. The theory describes the dynamics of an average particle represented by the kinetics of the particle's density function. The average particle, or the density function, is subjected to four fundamental processes as well as the conservation laws. These processes are thought to cause transport in an isotropic diffusive model. The four transport mechanisms are: 1) *diffusion* due to the irregular component of the heliospheric magnetic field; 2) *convection* due to the outflowing solar wind plasma that carries with it the frozen-in heliospheric magnetic field lines; 3) *drift* due to the large scale curvature and gradient of the regular component of the heliospheric magnetic field; and 4) *adiabatic energy loss* due to the diverging solar wind plasma. In our study, we ignore process 3) because drift effects play a small role in the transport of solar energetic particles to 1 AU [10]. We include the acceleration due to diffusion in momentum space and due to solar flare shock waves. Momentum loss terms important for the electrons due to synchrotron radiation and inverse Compton scattering are included in our analysis.

The mathematical model for this transport theory is written as a partial differential equation in time, momentum and space as:[11]

$$\frac{\partial f}{\partial t} = \frac{1}{r^2}\left[\frac{\partial}{\partial r} r^2 D_{rr} \frac{\partial f}{\partial r}\right] + \frac{1}{p^2}\left[\frac{\partial}{\partial p} p^2 D_{pp} \frac{\partial f}{\partial p} + p^2 \frac{dp}{dt} f\right] - \nabla_r \cdot \vec{V}_{sw} f + \frac{1}{3}\left(\nabla_r \cdot \vec{V}_{sw}\right) p \frac{\partial f}{\partial p} , \quad (1)$$

where $f(r,p,t)$ is the phase-space density function of the electrons depending on the radial position r and momentum p at time t, and D is the diffusion coefficient that depends on r and p. The density function is related to the observable electron differential spectrum j by:

$$j(r,p,t) = p^2 f(r,p,t) . \quad (2)$$

The first term in Equation 1 describes the spatial diffusion of electrons for a spherically symmetric diffusive process controlled by the radial diffusion coefficient D_{rr} :

$$D_{rr}(r,p) = D_{\parallel}(p) \cos^2(\psi) + D_{\perp}(p) \sin^2(\psi) , \quad (3)$$

where $D_{\parallel}(p)$ is the diffusion coefficient parallel to the magnetic field lines in the local solar wind frame, $D_{\perp}(p)$ is the diffusion coefficient perpendicular to the field lines and Ψ is the angle between the field line and the radial direction, given by:

$$\psi = \tan^{-1}\left[\frac{r\,\Omega_{\odot}}{V_{sw}(r)}\right] , \quad (4)$$

where $\Omega_{\odot}$ is the rotation speed of the sun about its axis (3×10^{-6} s^{-1}) and $V_{sw}(r)$ is the solar wind radial speed profile: [12]

$$V_{sw}(r) = \frac{2}{5} V_o \left[\frac{5}{2}\tanh\sqrt[3]{\frac{r}{10\,r_{\odot}}} - 1\right] , \quad (5)$$

where $r_{\odot}$ is the radius of the sun. Figure 1 shows a plot of Equation 5 with a value of V_o = 700 km/s. Note that the solar wind has a supersonic speed of 415 km/sec for $r \approx> 100\,r_{\odot}$.

From the quasi-linear theory for the heliospheric transport of energetic charged particles, the parallel diffusion coefficient can be written as: [9]

$$D_{\parallel}(p) = D_o R^{2-\zeta} \beta \left[\frac{B_e}{B(r)}\right] , \quad (6)$$

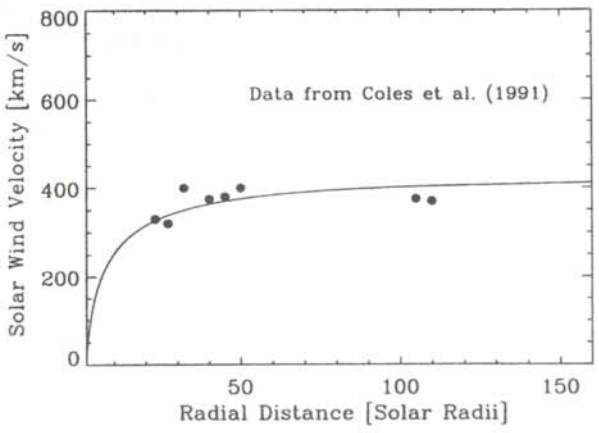

Figure 1

Solar wind speed as a function of radial distance plotted according to Equation 5. The data points are taken from Coles, W.A., et. al., J. Geophys. Res., 96, (1991), p. 13849.

where R is rigidity (the total momentum per charge), $\beta = v/c$ where v is the speed of the electron and c is the speed of light, and ζ is the spectral index of the fluctuating turbulent magnetic field.

The turbulence spectrum essentially is a plot of energy vs. frequency. In the so-called Kolmogorov spectrum, the plot follows a power law with an indes of -5/3, while for the so-called Kraichnan spectrum, the index is -3/2. In Equation 6, when the rigidity is expressed in units of giga Volts, D_o takes on a value of $\approx 10^{22}$ cm^2/s; $\zeta = 5/3$ for a purely Komlogorov spectrum and $\zeta = 1.5$ for a Kraichnan spectrum.

The last term in Equation 6, the ratio of the strength of the solar magnetic field at earth (which is around 50 μGauss) to the solar magnetic field at a position r is included to ensure that the electrons remain tied to the magnetic field lines. [13] $D_\perp$ is assumed to be a small fraction of $D_\parallel$.

The radial dependence of the solar magnetic field, $B(r)$, is taken to be: [14]

$$B(r) = \begin{cases} \dfrac{B_o}{r^2} & \text{for } r > r_f \\ B_f & \text{for } r \le r_f \end{cases} , \qquad (7)$$

where r_f is the radial extent of the solar flare ($\approx 10^{12}$ cm), and B_f is the strength of the solar magnetic field at the solar flare site (< 400 Gauss), and B_o is a constant.

The second term or acceleration term in Equation 1 describes diffusion in momentum space that is controlled by the diffusion coefficient, D_{pp}, which is independent of r or t. For a second-order Fermi acceleration mechanism, the dependence of the diffusion coefficient on the momentum is: [15]

$$D_{pp}(p) = \frac{\alpha\, p^2}{3\,\beta} , \qquad (8)$$

where α is a constant reflecting the efficiency of the acceleration process. A typical value for α is 0.025 s^{-1} in solar flare stochastic acceleration. [15]

The third term in Equation 1 describes the change in momentum of the electron. The losses are due to the motion of the electron in the ambient magnetic field (synchrotron radiation) as well as the interaction with the radiation field (inverse Compton scattering). These two momentum-loss terms are written as:[16]

$$\left.\frac{dp}{dt}\right|_{loss} = const\left[\frac{B^2(r)}{8\pi} + \rho(r)\right]\frac{\gamma^2}{\beta\, c} , \qquad (9)$$

where γ is the relativistic Lorentz factor for the electron and $\rho(r)$ is the photon density in the radiation field. The photon density in the radiation field is proportional to the ion density $\rho_i(r)$ given by:

$$\rho_i(r) = \begin{cases} \rho_o\left(\dfrac{r}{r_o}\right)^{-4.6} & \text{for } r > r_f \\ \rho_f & \text{for } r \le r_f \end{cases} , \qquad (10)$$

where ρ_o is a constant and ρ_f is the ion density at the flare site (10^9 cm^{-3}).

The momentum gain term is due to the shock or first order Fermi acceleration, given by [17]

$$\left.\frac{dp}{dt}\right|_{gain} = \frac{\kappa\, V_{sh}^{\,2}}{4\, D_\parallel}\, p , \qquad (11)$$

where κ is the volume filling factor of the shock waves and

$$V_{sh} = \sqrt{\frac{3\,k\,T_f}{m_p}}\; c \qquad (12)$$

is the shock speed, T_f the ambient temperature of the solar flare site, m_p the mass of the proton and k the Boltzmann constant.

The fourth and fifth terms (convection and adiabatic deceleration terms) describe the motion and momentum loss respectively due to an expanding plasma characterized by an expansion bulk velocity vector . The magnitude of the bulk velocity vector is given by Equation 5 and is radial:

$$\vec{V}_{SW}(\vec{r}) = V_{sw}(r)\ \hat{r} . \qquad (13)$$

To complete the mathematical model, one needs to specify physically meaningful initial and boundary conditions for f. At the flare site when $t = 0$, we assume f_o to be a Maxwellian distribution in p characterized by the temperature of the site T_f. The average thermal energy of the electrons prior to any acceleration or energy losses is assumed to be 3/2 $k\,T_f$. For boundary conditions, we let:

$$\begin{aligned} f &\to f_o \text{ as } r \to r_f \\ \frac{\partial f}{\partial r} &\to 0 \text{ as } r \to r_\infty . \end{aligned} \qquad (14)$$

In our case r_∞ is just a few AU.
For the boundary conditions in p, we let

$$\frac{\partial f}{\partial p} \to 0 \text{ as } p \to p_\infty \text{ and } p \to p_o , \qquad (15)$$

where p_o is a lower limit for p that is lower than the corresponding thermal energy and p_∞ is an upper limit for p at which f is unaffected by the transport process ($\approx 10^4$ keV/c).

NUMERICAL SOLUTION

We integrated Equation 1 using the numerical method of lines. [18] The time variable is kept "continuous" and a finite differencing scheme is applied to the other two variables at different points along a "time line" which is then integrated. The advantage of separating the time variable from the other two variables is that the stability issue of the solution is separated from the accuracy issue.

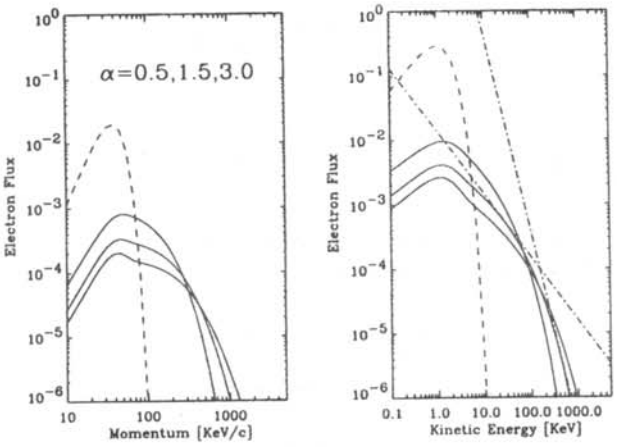

Figure 2

Electron flux as a function of momentum (left) and kinetic energy (right). The dashed line is the initial thermal distribution at the site of the solar flare corresponding to a site temperature of $T_f = 5x10^6$ K and a magnetic field strength of $B_f = 100$ Gauss. The solid lines are the steady state solutions to Equation 1 at 1 AU with efficiencies $\alpha =$ 0.5, 1.5, 3.0 min^{-1} (top to bottom). Dashed dotted straight lines (right) are fits corresponding to the $\alpha = 1.5$ min^{-1} case (the 'typical' flare case). The straight lines intersect around the electron kinetic energy of 150 keV.

Stability is an issue of concern for stiff partial differential equations, such as Equation 1, where the various terms have many orders of magnitude separation in strengths at widely separated radial and momentum points. Simple eigenvalue tests can reveal the stiffness of such equations.

All first-order and second-order diffusion related derivatives of f in the right hand side of Equation 1 are evaluated at a certain t using a five point centered differencing scheme accurate to fourth order. All first-order convection related derivatives are evaluated using a five point upwind or downwind biased differencing scheme. All field, diffusion and convection vector terms, along with their first and second order derivatives, are evaluated analytically. Once all of the derivatives of f are collected at all points along the time-line, they are integrated using the unconditionally stable and extremely efficient sparse Jacobian matrix techniques of Hindmarsh that is appropriate for stiff PDEs. [19] The accuracy in this integration scheme is completely determined by the user.

We used an (r,p) grid as a 37 x 37 matrix with logarithmically spaced points. This required the solving of 999 ODEs at all t points before time integration. The time integration essentially is solving a 999 x 999 sparse matrix. Due to the sparsity of the Jacobian matrix, only about 11,000 of almost 1 million total points needed to be evaluated, making this an most efficient algorithm. To reach a steady state solution required a mere 17 time steps from $t = 0$ to $t \approx 70$ min. This required less than 4 minutes of CPU time on a DEC-ALPHA 250 machine.

DISCUSSION

The output of our model was both transient and steady state solutions to the transport equation for the particular parameters used in that run. Figure 2 shows a plot of the original thermal distribution and the steady state solution at 1 AU vs. momentum and kinetic energy. The steady state solution at 1 AU exhibits the double power law which was previously found. [6] The break between the two power laws is in the same 100-200 keV range as the satellite data.

Figure 2 also shows results for two runs where the efficiency of the flare was altered. Lowering the efficiency drops the break into the 80-90 keV range, while raising it, pushes the break up to the 400 keV range. This

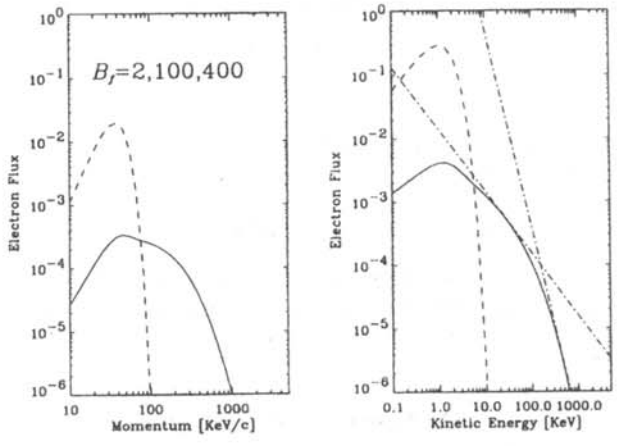

Figure 3

Same as Figure 2 but with $\alpha = 1.5$ min^{-1} and $B_f = 2$, 100, 400 Gauss. All solid lines (solutions at 1 AU) are essentially identical. 2 Gauss is a quiet time strength of the solar magnetic field at the solar surface. 400 Gauss is the maximum allowed strength according to hard x-ray and microwave observed emissions from the flares. [20]

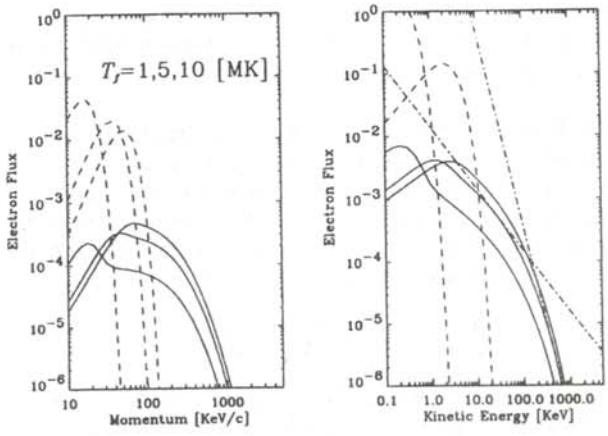

Figure 4

Same as Figure 2 but with $\alpha = 1.5$ min^{-1} and $T_f = 1,5,10$ MK (left to right). Solid lines are solutions at 1 AU.

seems to indicate that the break is a natural outgrowth of the efficiency of the flare in accelerating relativistic electrons rather that something caused by a separate acceleration mechanism.

The spectrum for a wide range of ambient magnetic field strengths (2 to 400 Gauss) is shown in Figure 3. The distributions show no variation from the 'typical ' flare graph with an efficiency of 1.5. This indicates that the strength of the magnetic field is not a factor in the position of the power law break.

Figure 4 shows the spectrum characteristic of a range of flare temperatures from 1 to 10 MK. For temperatures lower than 5 MK (that of a typical flare), the slope of both power laws decreases and the point of intersection moves down into the 50 keV region. For temperatures greater than 5 MV, the slopes increase, but the point of intersection remains in the 100 keV region. The temperature at the flare site is a rather sensitive parameter in the transport process. From independent results, we know the temperature of the flare site is not an entirely adjustable parameter.

Figure 5 shows the spectrum for electrons without the diffusive and shock accelerations, the two methods suggested in previous work. [6] Only the low energy electrons were affected by the shock in this case. The very low energy electrons gained energy as they diffused through the solar wind and the slightly higher energy electrons lost some energy. When the shock acceleration was omitted, there is no appreciable difference in the spectrum from the 'typical' flare solution. This suggests that diffusive acceleration is a dominant process in accelerating solar flare electrons. This indication is supported by the spectrum shown in Figure 6. This is spectrum at 1 AU for a 'typical' flare after only 5 minutes

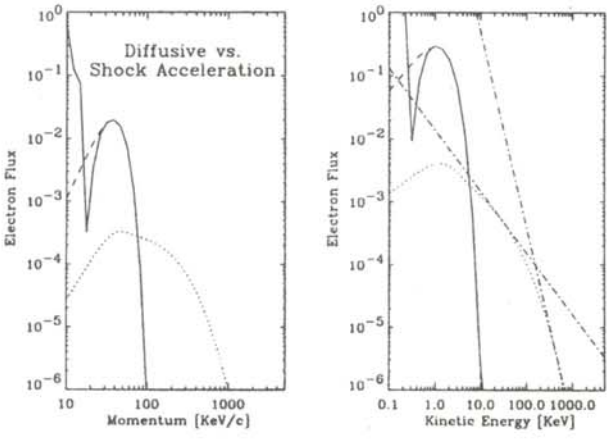

Figure 5

Same as Figure 2. The solid lines are solutions at 1 AU with no diffusive acceleration ($\alpha = 0$). Dotted lines are solutions at 1 AU with $\alpha = 1.5$ min^{-1} but with no shock acceleration. Both sets have $B_f = 100$ Gauss and $T_f = 5x10^6$ K.

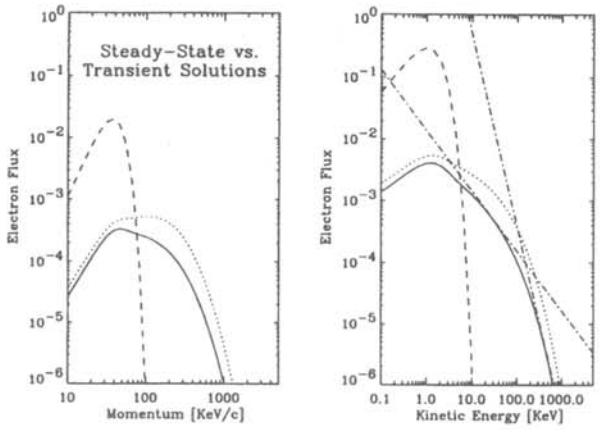

Figure 6

Same as Figure 2 for a typical flare ($\alpha = 1.5$ min^{-1}, $B_f = 100$ Gauss and $T_f = 5x10^6$K). Dotted lines are transient, after 5 minutes of onset of the flare, while the solid lines are steady state solutions at 1 AU.

rather than at the steady state time of approximately 70 minutes. The two spectra, one at 5 minutes and one in the steady state, are qualitatively similar other than that the shorter time solution has slightly more energy overall. This result indicates that the approach of the transport to equilibrium is quite rapid given that the typical duration of a solar flare is about 2 hours.

SUMMARY

Our analysis of both transient and steady state solutions at 1 AU of the transport equation show that:

- The observed break in the spectral index of solar flare electrons can be attributed to the acceleration efficiency of the dominant accelerating process at the flare site. This process is diffusive rather than one due to flare shock.

- The location of the break in the spectral index at 100-200 keV electron energy is quite sensitive to this efficiency, but is insensitive to other salient site parameters such as the strength of the ambient magnetic field.

- The rapid approach to steady state suggests that any second dominant acceleration mechanism would have to have a very short time scale and be very strong.

- We have identified the 'typical' flare to have an efficiency of 1.5 min^{-1} at a temperature of 5 MK. These values are almost independent of the strength of the ambient magnetic field and the site's ion and photon densities.

- Since the transport is inherently memory-less and approaches steady state rapidly, a second acceleration mechanism is not needed to describe the solar flare electron data. Such a mechanism is perhaps difficult to justify on both physical and mathematical grounds.

ACKNOWLEDGMENTS

The work has been supported in part by NASA-JOVE grant NAGS-1208. The author wishes to thank Dr. A.F. Barghouty for his continuous and diligent support. He also acknowledges the helpful and insightful input from the cosmic ray groups at the Naval Research Laboratory and Caltech.

REFERENCES

* Current address of author: Department of Physics and Astronomy, University of Denver, Denver, CO MIEdward@DU.edu.

1. Wild, J.P., Smerd, S.F. and Weiss, A.A., Ann. Rev. Astron. Astrophys., 1, (1963), p. 29.
2. Frost, K.J. and Dennis, B.R., Astrophys. J., 165, (1971), p. 655.
3. Lin, R.P., Solar Phys., 12, (1971), p. 209.
4. Lin, R.P. and Hudson, H.S., Solar Phys., 50, (1976), p. 153.
5. Bai, T. and Ramaty, R., Solar Phys., 49, (1976), p. 343.
6. Lin., R.P., Mewaldt, R.A., and Hollebeke, M.A.I., Astrophys. J., 253, (1982), p. 949.
7. Drury., L, Rep. Prog. Phys., 46, (1983), p. 973; Landford, R. and Eichler, D., Phys. Rep., 154, (1987), p. 1.
8. Gillespie, D.T., Markov Processes: An Introduction for Physical Scientists, (Academic Press, 1992).
9. Jokippi, J.R., Rev. Geophys. Sp. Phys., 9, (1971), p. 27.
10. Jokipii, J.R., Levy, E.H. and Hubbard, W.B., Astrophys. J., 213, (1976), p. 861.
11. Jokipii, J.R. and Parker, E.M., Astrophys. J., 160, (1970), p. 735.
12. Coles, W.A., Sp. Sc. Rev., 72, (1995), p. 211.
13. Morfill, G.E. and Völk, H.J., Geophys. Res., 84, (1979), p. 4446; Jokipii, J.R. and Davila, J.M., Astrophys. J., 248, (1981) p. 1156.
14. Parker, E.N., Interplanetary Dynamical Processes, (Wiley Interscience, 1963); Parker, E.N., Sp. Sc. Rev., 4, (1965), p. 666.; Dessler, A.J., Rev. Geophys., 5, (1967), p. 1.
15. Miller, J.A., Guessoum, N., and Ramaty, R., Astrophys. J., 361, (1990), p. 701.
16. Harwitt, M., Astrophysical Concepts, 2nd. ed., (Springer, 1988).
17. Schlickesier, R., Astron. and Astrophys., 143, (1985), p. 431.
18. Schiesser, W.E., The Numerical Method of Lines: Integration of Partial Differential Equations, (Academic Press, 1991).
19. Hindmarsh, A.C., Proc. IMACS Tenth World Congress, Montreal, Canada, (1982), p. 427; Byrne, G.D. and Hindmarash, A.C., J. Comp. Phys., 70, (1987), p. 1.
20. Holt, S.S. and Ramaty, R., Solar Phys., 8, (1969), p. 119.

FACULTY SPONSOR

Dr. A.F. Barghouty
Department of Physics
Roanoke College
Salem, VA 24153
barghouty@roanoke.edu, barghout@srl.Caltech.edu

PREPARING A MANUSCRIPT FOR PUBLICATION

Rexford E. Adelberger, Editor

Perhaps the most important thing for you to keep in mind when you write a manuscript which you intend to submit for publication to the Journal of Undergraduate Research in Physics is that the audience that will be reading the paper is junior or senior physics majors. They are knowledgeable about physics, but unlike you, they have not spent as much time trying to understand the specific work which is being reported in your paper. They also can read English well, and expect the paper to be written by a colleague, not a robot or an 'all-knowing' computer. There is a big difference between the comments you write in the margin of your lab notebook or what you might write in a technical brief and what you should present in a paper for publication in a scientific journal.

There is a significant difference between a Journal article and keeping a journal. Your laboratory data book should be the journal of what you did. It contains all the data, what you did (even if it was an attempt that turned out to be wrong), as well as comments as to what you were thinking at that time. The Journal article is an discussion of how you would do the research without excursions along blind alleys and hours spent collecting data that were not consistent. The reader does not have to be able to completely reproduce the work from the Journal article. The reader should be able to understand the physics and techniques of what was done.

How a person uses Journal articles to find out about new ideas in physics is often done in the following way. A computerized search, using key words in abstracts, is performed to find what work others have done in the area of interest. If the abstract seems to be about the question of interest, the body of the paper is tracked down and read. If the reader then wants to find out the finer details of how to reproduce the experiment or the derivation of some equation, the author of the paper is contacted for a personal in-depth conversation about the more subtle details.

The general style of writing that should be followed when preparing a manuscript for publication in the Journal is different from what you would submit to your English literature professor as a critique of some other work. The narrative of the paper is intended to do three things: 1) present the background necessary for the reader to appreciate and understand the physics being reported in the paper; 2) discuss the details of what you did and the implications of your work; 3) lead the reader through the work in such a way that they must come to the same concluding points that you did. When finished with your paper, the reader should not have to go back and try to decide for themselves what you did. Your narrative should lead them through your work in an unambiguous manner, telling them what to see and understand in what you did. The interpretation of the data or calculations should be done by the writer, not the reader. The interpretation of your results is the most important part of the paper.

You should take care to make sure that the material is presented in a concise logical way. You should make sure that your sentences do not have too many dependent clauses. Overly complicated sentences make the logic of an argument difficult to follow. You should choose a paragraph structure that focuses the attention of the reader on the development of the ideas.

A format which often achieves these aims is suggested below:

ABSTRACT : An abstract is a self contained paragraph that concisely explains what you did and presents any interesting results you found. The abstract is often published separately from the body of the paper, so you cannot assume that the reader of the abstract also has a copy of the rest of the paper. You cannot refer to figures or data that are presented in the body of the paper. Abstracts are used in computerized literature searches, so all key words that describe the paper should be included in the abstract.

INTRODUCTION: This is the section that sets the background for the important part of the paper. It is not just an abbreviated review of what you are going to discuss in detail later. This section of the narrative should present the necessary theoretical and experimental background such that a knowledgeable colleague, who might not be expert in the field, will be able to understand the data presentation and discussion. If you are going to use a particular theoretical model to extract some formation from your data, this model should be discussed in the introduction.

Where appropriate, factual information should be referenced using end-notes. When presenting background information, you can guide the reader to a detailed description of a particular item with the statement such as: *"A more detailed discussion of laminar flow can be found elsewhere [1]"*. If you know where there is a good discussion of some item, you don't have to repeat it, just guide the reader to the piece.

How one proceeds from this point depends upon whether the paper is about a theoretical study or is a report on an experiment. I will first suggest a format for papers about experimental investigations and then one that describes a theoretical derivation.

Experimental Investigations

THE EXPERIMENT: This section guides the reader through the techniques and apparatus used to generate the data. Schematic diagrams of equipment and circuits are often easier to understand than prose descriptions. A statement such as *"A diagram of the circuit used to measure the stopping potential is shown in Figure 6"* is better than a long elegant set of words. It is not necessary to describe in words what is shown in a diagram unless you feel that there is a very special part which should be pointed out to the reader. If special experimental techniques were developed as part of this work, they should be discussed here. You should separate the discussion of the equipment used to measure something from your results. This section should not include data presentations or discussions of error analysis.

DATA PRESENTATION AND INTERPRETATION OF RESULTS: This is the most important section of the paper. The data are the truths of your work. This section should lead the reader through the data and how errors were measured or assigned. The numerical data values are presented in tables and figures, each with its own number and caption, e.g.. *"The results of the conductivity measurements are shown in Table 3"*. It is difficult to follow narratives where the numerical results are included as part of the narrative. Raw, unanalyzed data should not be presented in the paper. All figures and tables should be referred to by their number. Any figure or table that is not discussed in the narrative should be eliminated. Items which are not discussed have no place in a paper.

A Theoretical Study

THE MODEL: This part should consist of a theoretical development of the constructs used to model the physical system

under investigation. Formulae should be on separate lines and numbered consecutively. The letters or symbols used in the equations should be identified in the narrative, e.g.. *The potential can be approximated as:*

$$W = Z - \sigma(\rho) \ , \qquad (1)$$

where Z is the number of protons and σ is the screening constant that is dependent on the charge density, ρ, of the inner electrons of the K and L shells. If you wish to use this formula at a later time in the narrative, you refer to it by its number, e.g.. "*The straight line fit shown in Figure 3 means that we can use Equation 1 to extract a value of...*"

CALCULATIONS: This section presents a summary and discussion of the numerical results calculated from the model. The results should be presented in tables or graphs, each with a caption. A table or graph that is not discussed in the narrative should be eliminated. Data that are not interpreted by the writer have no place in a paper. One should reference numerical results that are used in the calculations and come from previous work done by others .

The following sections pertain to both types of papers.

CONCLUSIONS: It is indeed rare that one can come to clear and meaningful conclusions in one paper. I do not know of many papers where this section should be included.

REFERENCES: All references, numbered in order from beginning to end of the paper, are collected together at the end of the paper. You should be aware of the following format:

If the reference is a text-

1. A.J. Smith and Q.C.S. Smythe, Electromagnetic Theory, Addison Wesley, New York, (1962), p. 168.

If the reference is a journal-

2. J. Boswain, Journal of Results, 92, (1968), pp. 122-127.

If the reference is unpublished-

3) R.J. Ralson, private communication.

ACKNOWLEDGMENTS: This short section should acknowledge the help received (that is not referenced in the previous section) from others. This is where you would give credit to a lab partner or someone in the machine shop who helped you build a piece of equipment.

OTHER ADVICE

TABLES AND FIGURES are placed by the layout editors at the corners of the page to make the format attractive and easy to read. Often a figure is not on the same page as the discussion of the figure. Each table or figure should be numbered and have a caption which explains the figure. Readers scan papers by looking at the figures and data tables before they read the narrative of the work. Take care to put enough information in the caption of a figure or table so that the reader can get some feeling for the meaning of the data presentation. All lines shown on graphs should be identified, e.g.. *"The dashed line is drawn to guide the eye"* or *"The solid line is a fit to the data using the Ising model"*

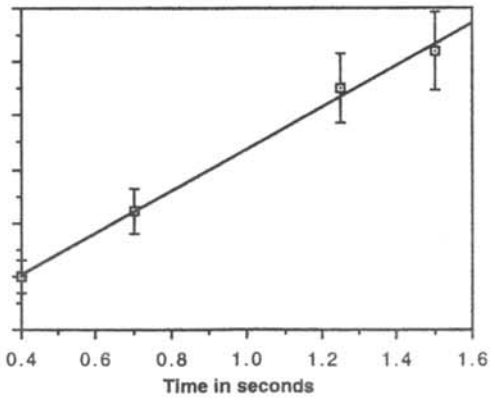

Figure 1

A graph of the measured thrust of a D-2 model rocket engine as a function of time. The line drawn is the least squares fit straight line to the data.

State	Experimental eV	Theoretical eV
3S	5.15±01	5.13
4S	1.89±02	1.93
3P	2.96±02	3.02

Table 1

Energy states found in the numerical search. The accepted values for these states are also listed.

An example of a graph of a set of data is shown in Figure 1. The graph is sized by the range of data points. The bottom left point does not have to be the point (0,0). Error bars are shown with the data points. A graph with all the data points clustered in one small corner and lots of white space does not help the reader get a feeling of the dependence of your data. Be careful that the figures you present are not too busy; too much information on a figure makes it difficult to pick out the important parts.

NUMBERS AND UNITS Any experimentally measured data presented in tables (such as shown in Table 1), should include an uncertainty. You should use scientific notation when presenting numbers, $(7.34 \pm .03) \times 10^7$ eV. Take care that you have the correct number of significant digits in your results; just because the computer prints out 6 digits does not mean that they are significant. You should use the MKS system of units.

STYLE It is often helpful to make a flow chart of your paper before you write it. In this way, you can be sure that the logical development of your presentation does not resemble two octopuses fighting, but that it is linear.

One generally writes the report in the past tense. You already did the experiment. You also should use the third person neuter case. Even though you might have done the work by yourself, you use "we". e.g.. *"We calculated the transition probability for..."* It is often confusing when you begin sentences with conjunctions. Make sure that each sentence is a clear positive statement rather than an apology.

There are a few words or phrases you should be careful of using. ***Fact*** - this is a legal word. I am not sure what it means in physics. ***Proof or prove*** - These words are meaningful in mathematics, but you can't prove something in physics, especially experimental physics. ***The purpose of this experiment is...*** Often it is necessary to do the experiment to complete the requirements for your degree. You do not need to discuss the purposes of the experiment. ***One can easily show that...*** - Don't try to intimidate the reader. What if the reader finds it difficult to show? Remember that the reader of your paper is a senior in college! ***It is obvious that... or One clearly can see....*** - Such statements only intimidate the reader that does not find your work trivial. What is obvious to someone who has spent a lot of time thinking about it may not be obvious to the reader of your paper. ***Data*** is the plural form of the noun datum. *"The data are ..."* or *"The data show that ...."*

The Journal of Undergraduate Research in Physics

The Journal of Undergraduate Research in Physics is the journal of Sigma Pi Sigma and the Society of Physics Students. It is published by the Physics Department of Guilford College, Greensboro NC 27410. Inquiries about the journal should be sent to the editorial office.

The Journal of Undergraduate Research in Physics ISSN 0731-3764

Editorial Office -
The Journal of Undergraduate Research in Physics
Physics Department
Guilford College
Greensboro, NC 27410
336-316-2279 (voice)
336-316-2951 (FAX)

Editor -
Dr. Rexford E. Adelberger
Professor of Physics
Physics Department, Guilford College
Greensboro, NC 27410
Rex@Guilford..Edu

Managing Editor -
Mr. Ari Betof
ABetof@Guilford.Edu

The Society of Physics Students

National Office -
Dr. Dwight Neuenschwander, Director
Ms. Sonja Lopez, SPS Supervisor
Society of Physics Students
American Institute of Physics
1 Physics Ellipse
College Park, MD 20740
301-209-3007

President of the Society -
Dr. Robert Fenstermacher
Department of Physics
Drew University

President of Sigma Pi Sigma -
Dr. Jean Krisch
Department of Physics
University of Michigan, Ann Arbor